Finite Elements in Analysis and Design 241 (2024) 104221

Contents lists available at ScienceDirect

Finite Elements in Analysis & Design

journal homepage: www.elsevier.com/locate/finel

Finite element model to investigate the dynamic instability of ring stiffened conical shells subjected to flowing fluid

Mohammadamin Esmaeilzadehazimi *, Aouni A. Lakis, Mohammad Toorani

Mechanical Engineering Department, Ecole Polytechnique de Montréal, C.P. 6079, Succ. Centre-ville, Montréal, H3C 3A7, Canada

ARTICLE INFO

Keywords:
Finite element method
Fluid–structure interaction
Conical shell
Static divergence
Ring stiffeners

ABSTRACT

In this study, the vibration stability (i.e., static divergence) and critical velocity of fluid-conveying, ring-stiffened, truncated conical shells are investigated under various boundary conditions. The shell is characterized using Sanders' theory, while the fluid is modeled using a velocity potential approach with the impermeability condition at the fluid-shell interface. Using linear superposition, the natural frequencies corresponding to each flow velocity are determined by satisfying the dynamic characteristic equation and boundary conditions. Critical velocities are identified where the natural frequencies vanish, indicating static divergence. Parametric studies are conducted to investigate the effect of ring stiffeners on the critical velocities with respect to the semi-cone angle, number of rings, and boundary conditions. The proposed model is validated through comparison with published data. It is found that the rings significantly affect the stability of the cone under different boundary conditions. Instability in stiffened shells occurs at higher critical fluid velocities than in unstiffened shells across all boundary conditions. An increase in the vertex angle leads to a decrease in critical flow discharge.

1. Introduction

The vibrational characteristics of shells, which are widely used in various industries, have been extensively studied in both vacuum and when exposed to stationary fluids. Conical shells have been thoroughly investigated in various dynamic scenarios, such as examining material properties, analyzing thickness ratios, considering hydrostatic pressure effects, and exploring vibration modes. These aspects have been addressed in Refs. [1–5].

Incorporating stiffeners is a common practice in shell design in order to enhance structural integrity. While there has been extensive research on ring-stiffened cylindrical shells [6–8], conical shells have received comparatively less attention. The analysis of stiffeners typically falls into two categories: the smeared-out method and the discrete-element approach. In the former method, the uniform distribution of equally sized stiffeners is crucial for effective implementation. While a few studies have analyzed ring-stiffened conical shells under fluid loading [9,10], most research has focused on the vibration analysis of stiffened conical shells in vacuo [11–15]. Xie et al. [16] and Liu et al. [17] addressed the problem of analyzing the vibration behavior of conical shells influenced by fluid loading and ring stiffeners. Xie's approach involved dividing the shell into segments, considering classical and elastic boundary conditions, and treating the shell as locally cylindrical strips to account for fluid effects. They used discrete ring stiffeners and employed Flügge theory to model shell and stiffener motion. In contrast, Liu adopted a different strategy using the transfer matrix method for vibration analysis. Liu's study focused on conical shells with variable thickness and employed the smeared approach to address stiffeners. While both approaches sought to predict the natural frequencies of these shells, they employed distinct

* Corresponding author.
E-mail address: mohammadamin.esmaeilzadehazimi@polymtl.ca (M. Esmaeilzadehazimi).

https://doi.org/10.1016/j.finel.2024.104221
Received 29 February 2024; Received in revised form 15 June 2024; Accepted 19 July 2024
Available online 31 July 2024

methods, boundary conditions, and approaches to modeling stiffeners. The authors' most recent study [18] examined the impact of ring stiffeners on the natural frequency of fluid-filled conical shells using a method that is detailed later in this paper.

Fluid-conveying thin shells are susceptible to three primary types of instabilities: static divergence, flutter, and dynamic divergence (oscillatory instabilities). Oscillatory instabilities, in particular, are highly critical as they can result in catastrophic failures caused by fatigue. It is essential to differentiate dynamic divergence from flutter, as flutter is characterized by a distinct oscillation frequency at its initiation. Previous studies have developed models to analyze these instabilities in structures, with a predominant focus on cylindrical shells or pipes supported by various types of elastic foundations and supports [19–31]. These studies have employed diverse methodologies and shell theories to derive equations of motion and address the effects of fluid pressure. Numerous system parameters that impact stability have been extensively investigated. The axial flow, which can be external, internal, or annular, is typically modeled using potential theory for inviscid and incompressible fluids. These studies consistently demonstrate that eigenfrequencies of shells coupled with internal or external flows tend to decrease monotonically as flow speed increases. Initially, the frequencies are minimally affected by increases in flow speed; however, as the shell approaches instability (divergence at zero frequency), the frequencies exhibit a sharp decline with increasing flow velocity. Furthermore, the vibrational modes of the shell in the presence of flow are complex. The real part of the nondimensional eigenfrequency, which is proportional to damping, indicates stability: a positive real part suggests instability, while a negative real part indicates stability. The critical point of static divergence occurs when the lowest frequency curve reaches zero. Restabilization of the system is indicated by the intersection of the second frequency curve with zero. The convergence of the first and second mode curves marks the onset of coupled-mode flutter (also known as Païdoussis-type flutter [32]), as depicted by the emergence of a branch from the curve corresponding to the second mode. It is crucial to note that coupled-mode flutter, involving significant shell deformations, typically cannot be conclusively determined through linear theory alone [19].

As mentioned in previous studies, the main focus has been on the vibrations of conical shells, either in a vacuo or when immersed in fluids. However, these studies do not consider the dynamics of fluid flow. Lakis et al. [33] conducted a dynamic analysis of anisotropic conical shells filled with fluid. They used a hybrid finite element (FEM) method and classical shell theory to determine displacement functions. Although they incorporated flow-related terms, their research was only applicable to quiescent fluids. Kumar and Ganesan [34] subsequently introduced a semi-analytical finite element approach that combined structural equations based on the first-order shear deformation theory with a fluid model based on velocity potential to analyze elastic conical shells carrying fluids. They discretized the fluid domain using an eight-noded annular ring element. Their investigation addressed conical shells with various cone angles and boundary conditions, revealing instability at a critical fluid velocity corresponding to the shell's lowest natural frequency. Kerboua et al. [35] used a hybrid FEM, originally introduced by Lakis et al. [33], to analyze the vibrations of conical shells containing internal flowing fluids. They observed that the solution closely matched the semi-analytical solution presented by Kumar and Ganesan [34], except in cases of critical velocities. Bagheri et al. [36] analyzed shear deformable conical shells with intermediate ring support using the first-order shear deformation theory and generalized differential quadratures (GDQ). Their study, which included parametric analyses, divided the shell into two sections with continuity at the ring to explore natural frequencies. Zarei et al. [37] investigated the vibration characteristics of composite conical shells reinforced with bevel stiffeners using experimental, analytical, and numerical methods. They derived governing equations using shear deformation theory and the Ritz method, which were validated through experiments. Recent research has explored the combined behavior of stiffened and unstiffened conical-cylindrical shells as reported by [38–40], as well as various aspects of graphene nanoplatelet-reinforced composites, focusing on the vibration and buckling responses under different stiffening and boundary conditions using advanced computational models as described by [41–43]. Zghal et al. [44–52] have extensively studied functionally graded materials (FGMs) and carbon nanotube-reinforced composites (CNTRCs) in shell structures. These studies have investigated the static and dynamic behavior, buckling phenomena, and incorporating geometrical nonlinearity using first-order shear deformation theory (FSDT) to account for transverse shear deformations.

Based on the literature review, it was found that no prior studies have investigated the dynamic behavior of ring stiffened conical shells conveying fluid, to the best of the authors' knowledge. In order to fill this research gap, our study builds upon the work conducted by Kumar and Ganesan [34]. We employed a hybrid finite element method that integrates classical thin shell theory with a truncated cone element. Displacement functions were derived from Sanders' thin shell equations. To effectively describe the fluid–structure interaction caused by small shell displacements, linear potential flow theory was utilized. The velocity potential function, Bernoulli's equation, and an impermeability condition were used to determine the pressure distribution, enabling the computation of three fluid forces exerted by the moving fluid on the structure's wall. The unique features of this study, to the authors' knowledge, are as follows: (i) the primary objective of this study is to introduce a simplified approach to determine the natural frequencies and critical velocities corresponding to zero natural frequency, which indicates the occurrence of static divergence in fluid conveying stiffened conical shells. This approach can be extended to ring stiffened cylindrical shells; (ii) the first comparison made between two studies examining the effects of internal flowing fluid on stiffened and unstiffened shells; (iii) modification of the elasticity matrix to account for the influence of internal/external rings by incorporating their height into the shell thickness. Additionally, the comprehensive analysis takes into consideration the geometric shape, boundary conditions, and the number of rings, allowing for the identification of stability margins and critical fluid velocities.

2. Structural model

2.1. Equilibrium equations

The geometric characteristics of a truncated conical shell are illustrated in Fig. 1. This shell displays varying thicknesses h and is bounded by circular nodes labeled i and j, which represent the small and large ends of the shell, respectively. The positions along

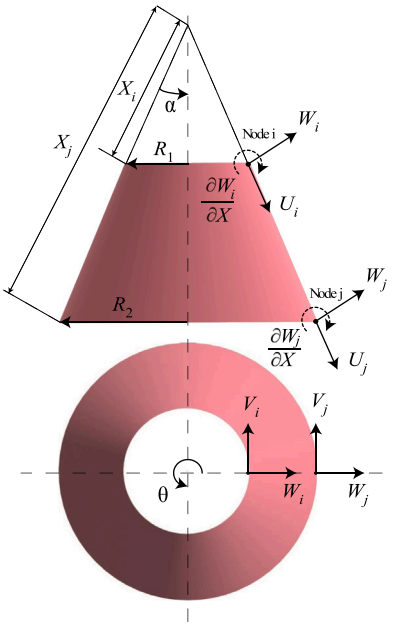

Fig. 1. Schematic of a conical shell and the corresponding degrees of freedom.

the X-axis, referred to as meridional coordinates, are measured starting from the middle of the conical section at nodes i and j. The small and large end radii are denoted as R_1 and R_2, respectively, with an X-direction length of L and a semi-vertex angle of α. Additionally, a circumferential coordinate θ is employed. The structure is modeled using a finite element method, with four degrees of freedom at each node: one rotation ($\partial W/\partial x$) and three displacements (U, V, W) in the axial, tangential, and radial directions, respectively. The displacement vector at node i, denoted as $\boldsymbol{\delta}_i$, is determined by the following equation:

$$\{\boldsymbol{\delta}_i\} = \begin{Bmatrix} U_i & W_i & \partial W_i/\partial x & V_i \end{Bmatrix}^{\mathrm{T}}. \tag{1}$$

The nodal displacement vector $\boldsymbol{\delta}$ for finite elements with n nodes can be expressed as follows:

$$\{\boldsymbol{\delta}\} = \left\{ \{\boldsymbol{\delta}_1\}^{\mathrm{T}}, \{\boldsymbol{\delta}_2\}^{\mathrm{T}}, \ldots, \{\boldsymbol{\delta}_n\}^{\mathrm{T}} \right\}^{\mathrm{T}}. \tag{2}$$

Based on Sanders' thin shell theory [53], the equilibrium equations for a conical shell can be expressed as follows:

$$L_1 = N_x \sin(\alpha) + x \sin(\alpha) \left(\frac{\partial}{\partial x} N_x \right) + \frac{\partial}{\partial \theta} N_{x\theta} - N_\theta \sin(\alpha) - \frac{\cos(\alpha)}{2x \sin(\alpha)} \left(\frac{\partial}{\partial \theta} M_{x\theta} \right), \tag{3a}$$

$$L_2 = \frac{3\cos(\alpha)\left(\frac{\partial}{\partial x} M_{x\theta}\right)}{2} + \frac{\cos(\alpha)\left(\frac{\partial}{\partial \theta} M_\theta\right)}{x \sin(\alpha)} + 2\sin(\alpha) N_{x\theta} + x \sin(\alpha) \left(\frac{\partial}{\partial x} N_{x\theta} \right) + \frac{\partial}{\partial \theta} N_\theta + \frac{3\cos(\alpha) M_{x\theta}}{2x}, \tag{3b}$$

$$L_3 = \frac{2\left(\frac{\partial}{\partial \theta} M_{x\theta}\right)}{x} + \frac{\frac{\partial^2}{\partial \theta^2} M_\theta}{x \sin(\alpha)} - \left(\frac{\partial}{\partial x} M_\theta \right) \sin(\alpha) + x \sin(\alpha) \left(\frac{\partial^2}{\partial x^2} M_x \right) + 2\sin(\alpha) \left(\frac{\partial}{\partial x} M_x \right) + 2 \frac{\partial^2}{\partial \theta \partial x} M_{x\theta} - N_\theta \cos(\alpha). \tag{3c}$$

Where N_x, N_θ, and $N_{x\theta}$ correspond to the membrane forces, while M_x, M_θ, and $M_{x\theta}$ refer to the bending moments. The detailed mathematical formulations can be found in the study by [18].

2.2. Strain–displacement relations

The relationship between displacement and strains for a conical shell is defined by the following equation:

$$\begin{Bmatrix} \epsilon_x \\ \epsilon_\theta \\ 2\bar{\epsilon}_{x\theta} \\ \kappa_x \\ \kappa_\theta \\ \bar{\kappa}_{x\theta} \end{Bmatrix} = \begin{Bmatrix} \frac{\partial U}{\partial x} \\ \frac{1}{x\sin(\alpha)} \frac{\partial V}{\partial \theta} + \frac{U}{x} + \frac{W\cot(\alpha)}{x} \\ \frac{\partial V}{\partial x} + \frac{1}{x\sin(\alpha)} \frac{\partial U}{\partial \theta} - \frac{V}{x} \\ -\frac{\partial^2 W}{\partial x^2} \\ \frac{\partial V}{\partial \theta} \frac{\cos(\alpha)}{x^2 \sin^2(\alpha)} - \frac{1}{x^2 \sin^2(\alpha)} \frac{\partial^2 W}{\partial \theta^2} - \frac{\partial W}{\partial x} \frac{1}{x} \\ -\frac{2}{x\sin(\alpha)} \frac{\partial^2 W}{\partial x \partial \theta} + \frac{3}{2} \frac{\cot(\alpha)}{x} \frac{\partial V}{\partial x} - \frac{\partial U}{\partial \theta} \frac{\cos(\alpha)}{2x^2 \sin^2(\alpha)} + \frac{2\sin(\alpha)}{x^2 \sin^2(\alpha)} \frac{\partial W}{\partial \theta} - \frac{3}{2} \frac{\cot(\alpha)}{x^2} V \end{Bmatrix}, \tag{4}$$

2.3. Elasticity matrix and ring-stiffeners model

The elasticity matrix of a conical shell is defined as [54]:

$$\begin{bmatrix} N_x \\ N_\theta \\ N_{x\theta} \\ M_x \\ M_\theta \\ M_{x\theta} \end{bmatrix} = \underbrace{\begin{bmatrix} A_{11}^* & A_{12}^* & A_{16}^* & B_{11}^* & B_{12}^* & B_{16}^* \\ A_{12}^* & A_{22}^* & A_{26}^* & B_{12}^* & B_{22}^* & B_{26}^* \\ A_{16}^* & A_{26}^* & A_{66}^* & B_{16}^* & B_{26}^* & B_{66}^* \\ B_{11}^* & B_{12}^* & B_{16}^* & D_{11}^* & D_{12}^* & D_{16}^* \\ B_{12}^* & B_{22}^* & B_{26}^* & D_{12}^* & D_{22}^* & D_{26}^* \\ B_{16}^* & B_{26}^* & B_{66}^* & D_{16}^* & D_{26}^* & D_{66}^* \end{bmatrix}}_{[P]} \begin{bmatrix} \varepsilon_x \\ \varepsilon_\theta \\ 2\bar{\varepsilon}_{x\theta} \\ \kappa_x \\ \kappa_\theta \\ \bar{\kappa}_{x\theta} \end{bmatrix}. \tag{5}$$

$[A^*], [B^*]$, and $[D^*]$ are matrices referred to as the extensional, coupling, and bending stiffness, respectively. These matrices are defined by [55] as follows:

$$A_{ij}^* = \sum_{k=1}^{n} \left[(\bar{Q}_{ij})\right]_k \left(h_k - h_{k-1}\right), \qquad i = 1,2,6; \qquad j = 1,2,6 \tag{6a}$$

$$B_{ij}^* = \frac{1}{2}\sum_{k=1}^{n} \left[(\bar{Q}_{ij})\right]_k \left(h_k^2 - h_{k-1}^2\right), \qquad i = 1,2,6; \qquad j = 1,2,6 \tag{6b}$$

$$D_{ij}^* = \frac{1}{3}\sum_{k=1}^{n} \left[(\bar{Q}_{ij})\right]_k \left(h_k^3 - h_{k-1}^3\right), \qquad i = 1,2,6; \qquad j = 1,2,6. \tag{6c}$$

Where $\bar{Q}_{ij}$ are referred to as the elements of the transformed reduced stiffness matrix $[\bar{Q}]$, and they are given by [55]:

$$\bar{Q}_{11} = q_{11}c^4 + q_{22}s^4 + 2\left(q_{12} + 2q_{66}\right)s^2c^2, \tag{7a}$$

$$\bar{Q}_{12} = \left(q_{11} + q_{22} - 4q_{66}\right)s^2c^2 + q_{12}\left(c^4 + s^4\right), \tag{7b}$$

$$\bar{Q}_{22} = q_{11}s^4 + q_{22}c^4 + 2\left(q_{12} + 2q_{66}\right)s^2c^2, \tag{7c}$$

$$\bar{Q}_{16} = \left(q_{11} - q_{12} - 2q_{66}\right)c^3s - \left(q_{22} - q_{12} - 2q_{66}\right)s^3c, \tag{7d}$$

$$\bar{Q}_{26} = \left(q_{11} - q_{12} - 2q_{66}\right)cs^3 - \left(q_{22} - q_{12} - 2q_{66}\right)c^3s, \tag{7e}$$

$$\bar{Q}_{66} = \left(q_{11} + q_{22} - 2q_{12} - 2q_{66}\right)s^2c^2 + q_{66}\left(s^4 + c^4\right). \tag{7f}$$

Where $c = \cos(\theta_p)$ and $s = \sin(\theta_p)$, with θ_p representing the angle of each ply as shown in Fig. 2, and q_{ij} denoting the reduced stiffness coefficients, which are defined as follows:

$$q_{11} = \frac{E_1}{1 - \upsilon_{21}\upsilon_{12}}, \tag{8a}$$

$$q_{12} = \frac{\upsilon_{12}E_2}{1 - \upsilon_{21}\upsilon_{12}}, \tag{8b}$$

$$q_{22} = \frac{E_2}{1 - \upsilon_{21}\upsilon_{12}}, \tag{8c}$$

$$q_{66} = G_{12}. \tag{8d}$$

E_1, and E_2 are the longitudinal and transverse Young's moduli in directions 1 and 2, respectively. υ_{12} is the major Poisson's ratio, and G_{12} is the in-plane shear modulus (in plane 1–2). By knowing the thickness, t_k, of each ply, we can obtain the coordinates of the top and bottom of each ply and compute the last remaining variable, h_k, in Eqs. (6). Consider a laminate made of n plies shown in Fig. 2 where each ply has a thickness of t_k. Therefore, the total thickness of the laminate, h, is:

$$h = \sum_{k=1}^{n} t_k. \tag{9}$$

The mid-plane is positioned at a distance of $h/2$ from either the upper or lower surface of the laminate, both without the presence of stiffeners and when ring stiffeners are uniformly distributed along the mid-plane.

Ply 1:	Ply k: $(k = 2, 3, \ldots n-2, n-1)$	Ply n:
$h_0 = -\frac{h}{2}$ (top surface),	$h_{k-1} = -\frac{h}{2} + \sum_{=1}^{k-1} t$(top surface),	$h_{n-1} = \frac{h}{2} - t_n$ (top surface) ,
$h_1 = -\frac{h}{2} + t_1$(bottom surface),	$h_k = -\frac{h}{2} + \sum_{=1}^{k} t$ (bottom surface) ,	$h_n = \frac{h}{2}$ (bottom surface) .

(10)

In the current theoretical calculations, the shell is divided into a total of $(2N_r + 1)$ finite elements, where N_r represents the number of rings distributed along the circumference of the shell. Each segment of the shell comprises both stiffened and unstiffened sections,

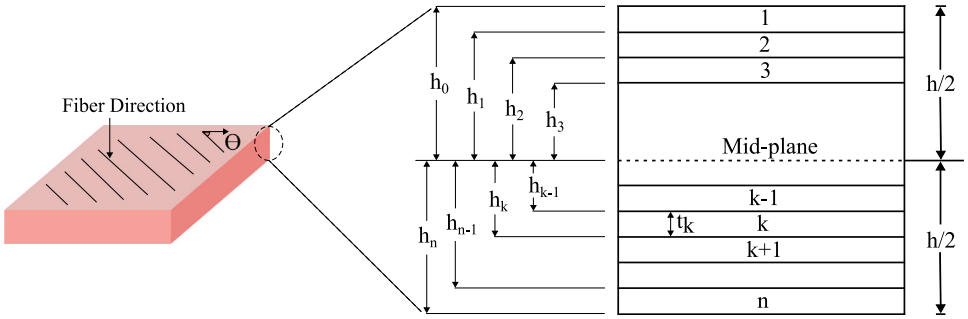

Fig. 2. Schematic of a laminate, showing h_k coordinates of each ply.

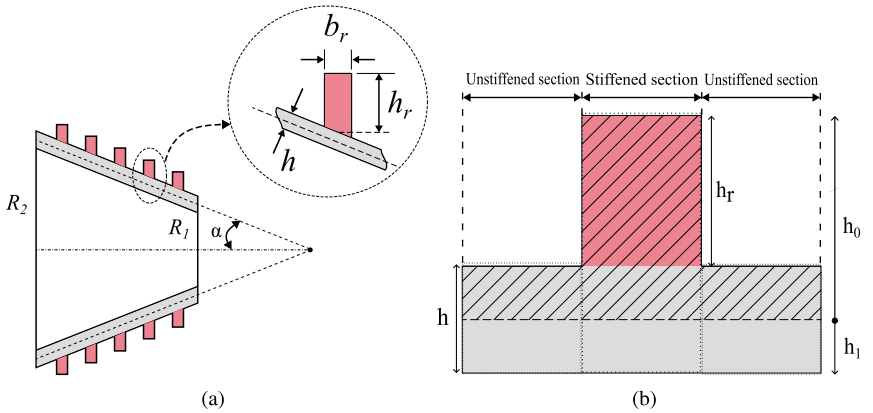

Fig. 3. (a) Geometry of the ring, (b) Coordinates of the top and bottom ply of the homogeneous material.

with the mean radii differences between these sections taken into account. In order to accurately represent the circumferentially distributed ring stiffeners, modifications to Eqs. (10) are required, depending on whether the rings are internal or external. For external rings, the height of the ring is added to the top of the mid-plane, while for internal rings, it is added to the bottom. It is important to note that while the proposed method effectively captures the effects of symmetrically distributed rings along the shell, the proposed method is constrained in its capacity to simulate the impacts of longitudinally distributed stringers.

For isotropic external rings, with the angle of the ply equal to zero, $E_1 = E_2 = E$ and $\upsilon_{12} = \upsilon_{21} = \upsilon$, the formulation is presented as follows (see Fig. 3).

$$h_0 = -\frac{h}{2} + h_r \text{ (top surface)}, \tag{11a}$$

$$h_1 = \frac{h}{2} \text{ (bottom surface)}, \tag{11b}$$

Determining the thickness, h, of the shell, as well as the coordinates of its top and bottom surfaces, h_i where i ranges from 1 to 2, facilitates the derivation of Eq. (11). This equation is dependent on whether the element is reinforced with a ring or not. Subsequently, by employing the matrices $[\bar{Q}]$ and the surface coordinates, the stiffness matrices $[A^*]$, $[B^*]$, and $[D^*]$ can be computed using Eq. (6) for isotropic materials. Therefore, the elastic properties of an isotropically optimized conical shell are described as follows:

$$\begin{bmatrix} N_x \\ N_\theta \\ N_{x\theta} \\ M_x \\ M_\theta \\ M_{x\theta} \end{bmatrix} = \underbrace{\begin{bmatrix} A^*_{11} & A^*_{12} & 0 & B^*_{11} & B^*_{12} & 0 \\ A^*_{12} & A^*_{22} & 0 & B^*_{12} & B^*_{22} & 0 \\ 0 & 0 & A^*_{66} & 0 & 0 & B^*_{66} \\ B^*_{11} & B^*_{12} & 0 & D^*_{11} & D^*_{12} & 0 \\ B^*_{12} & B^*_{22} & 0 & D^*_{12} & D^*_{22} & 0 \\ 0 & 0 & B^*_{66} & 0 & 0 & D^*_{66} \end{bmatrix}}_{[P]} \begin{bmatrix} \varepsilon_x \\ \varepsilon_\theta \\ 2\bar{\varepsilon}_{x\theta} \\ \kappa_x \\ \kappa_\theta \\ \bar{\kappa}_{x\theta} \end{bmatrix}. \tag{12}$$

2.4. Equations of motion

By substituting Eq. (6) into Eq. (12) and then introducing them into Eq. , a set of equations of motion can be derived in terms of displacements of the mean surface of the shell and material properties. These equations can be expressed as follows:

$$L_1\left(U, W, V, P_{ij}\right) = 0, \tag{13a}$$

$$L_2\left(U, W, V, P_{ij}\right) = 0, \tag{13b}$$

$$L_3\left(U, W, V, P_{ij}\right) = 0. \tag{13c}$$

Where L_k (k = 1, 2, 3) represents three linear differential operators, whose specific forms are provided in Ref. [18]. Additionally, the P_{ij} terms, which form the matrix $[P]$ of order 6×6, are defined in Eq. (12).

2.5. General solution of equations of motion to find the displacement

The geometric properties of this element facilitate the application of the complete equilibrium equations in order to derive displacement functions that depend on nodal displacements. In the case of motions associated with the nth circumferential wave number, the displacement functions can be represented by a Fourier series in the following manner:

$$\begin{Bmatrix} U(x,\theta) \\ W(x,\theta) \\ V(x,\theta) \end{Bmatrix} = \sum_{n=0}^{\infty} [T] \begin{Bmatrix} u_n(x) \\ w_n(x) \\ v_n(x) \end{Bmatrix}, \tag{14}$$

where n is the number of circumferential modes, and u_n, w_n, v_n are the magnitudes of the displacements and depend only on x. [T] is a (3×3) matrix in θ, given by:

$$[T] = \begin{bmatrix} \cos n\theta & 0 & 0 \\ 0 & \cos n\theta & 0 \\ 0 & 0 & \sin n\theta \end{bmatrix}. \tag{15}$$

By substituting Eq. (14) with Eq. (13), we obtain three standard homogeneous differential equations for $u_n(x)$, $w_n(x)$, and $v_n(x)$. The solutions to these differential equations can be expressed in a general form:

$$\begin{Bmatrix} u_n(x) \\ w_n(x) \\ v_n(x) \end{Bmatrix} = \left(\frac{x}{l_e}\right)^{\frac{\lambda-1}{2}} \begin{Bmatrix} \bar{A} \\ \bar{B} \\ \bar{C} \end{Bmatrix}, \tag{16}$$

where λ, A, B, and C are complex numbers, and l_e is an arbitrary reference length, i.e., the midpoint of the finite conical element. By introducing $u_n(x), w_n(x)$, and $v_n(x)$ in Eq. (13), a system of three ordinary linear equations in $\bar{A}$, $\bar{B}$, and $\bar{C}$ can be obtained. This system of equations can then be rearranged and represented in matrix form:

$$[H] \begin{Bmatrix} \bar{A} \\ \bar{B} \\ \bar{C} \end{Bmatrix} = \begin{bmatrix} H_{11} & H_{12} & H_{13} \\ H_{21} & H_{22} & H_{23} \\ H_{31} & H_{32} & H_{33} \end{bmatrix} \begin{Bmatrix} \bar{A} \\ \bar{B} \\ \bar{C} \end{Bmatrix} = \begin{Bmatrix} 0 \\ 0 \\ 0 \end{Bmatrix}. \tag{17}$$

$[H]$ is a square matrix of size (3×3) with elements that are dependent on the parameter λ as mentioned in Ref. [18]. In order to obtain a nontrivial solution, the determinant of matrix $[H]$ must be equal to zero, leading to the following characteristic equation:

$$h_8\lambda^8 + h_6\lambda^6 + h_4\lambda^4 + h_2\lambda^2 + h_0 = 0. \tag{18}$$

The roots of Eq. (18) can be expressed as $\lambda_j = \pm k_j \pm i\mu_j$. Each root represents a solution to the linear equations of motion in Eq. (13). The number of distinct roots of the characteristic polynomial determines the degrees of freedom of the element. For isotropic materials, there are eight distinct roots, corresponding to eight degrees of freedom. To account for the presence of these distinct roots, the complete solution is assumed to be the sum of all eight roots, each with its set of constants $\bar{A}_j, \bar{B}_j, \bar{C}_j$ (where j = 1..8).

$$u_n(x) = \sum_{k=1}^{8} \bar{A}_j y^{\lambda_j - 1}, \tag{19a}$$

$$w_n(x) = \sum_{k=1}^{8} \bar{B}_j y^{\lambda_j - 1}, \tag{19b}$$

$$v_n(x) = \sum_{k=1}^{8} \bar{C}_j y^{\lambda_j - 1}. \tag{19c}$$

Where y is the dimensionless ratio x/l_e, as defined in Eq. (16). The independent constants $\bar{A}_j$ and $\bar{B}_j$ can be expressed in terms of $\bar{C}_j$.

$$\bar{A}_j = \alpha_j \bar{C}_j, \quad \bar{B}_j = \beta_j \bar{C}_j, \quad j = 1, 2, \ldots, 8 \tag{20}$$

Here, α_j and β_j are complex numbers. By substituting Eq. (20) into Eq. (17), we can determine the values of α_j and β_j using the following procedure:

$$\begin{bmatrix} H_{11} & H_{12} \\ H_{21} & H_{22} \end{bmatrix} \begin{Bmatrix} \alpha_j \\ \beta_j \end{Bmatrix} = \begin{Bmatrix} -H_{13} \\ -H_{23} \end{Bmatrix}. \tag{21}$$

The terms H_{ij} represent the elements of matrix $[H]$ in Eq. (17). The expressions for the functions $u_n(x), w_n(x)$, and $v_n(x)$ can be expressed in their final form as follows:

$$\begin{Bmatrix} u_n(x) \\ w_n(x) \\ v_n(x) \end{Bmatrix} = [R]\{c^*\}. \tag{22}$$

$[R]$ is a matrix of dimensions 3×8, with its elements expressed in the following format:

$$\left[R_{i,j}\right]_{3\times 8} = \left(\sqrt{\frac{x}{l_e}}\right)^{\lambda_j - 1} \chi, \tag{23}$$

χ varies depending on the index i. For radial displacement, χ is set to 1. However, for axial displacement (U, $i = 1$) and tangential displacement (V, $i = 3$), χ becomes complex numbers. The values of α and β define χ (refer to Eq. (21)). More details about the matrix $[R]$ can be found in Ref. [18]. The constants $\{c^*\} = \left\{C_1^*, \ldots, C_8^*\right\}^T$ are the only variables that are not fixed in the problem. To determine them, eight boundary conditions are required, four at each end of the cone. The displacement vector for the circumferential mode, n, at point (x, θ) can be expressed as follows:

$$\begin{Bmatrix} U(x,\theta) \\ W(x,\theta) \\ V(x,\theta) \end{Bmatrix} = [T][R]\{c^*\}. \tag{24}$$

By employing Eqs. (1) and (2), it is now possible to define the displacement function.

$$\{\delta\} = \{\delta_i, \delta_j\}^T = \left\{u_{ni}, w_{ni}, \partial w_{ni}/\partial x, v_{ni}, u_{nj}, w_{nj}, \partial w_{nj}/\partial x, v_{nj}\right\}^T = [A]\{C\}. \tag{25}$$

The elements within the matrix $[A]$ can be obtained by substituting x with the nodal coordinates x_i and x_j, which correspond to nodes i and j, respectively. The vector $\{C\}$ can be determined by multiplying the matrix $[A]$ with its inverse.

$$\{C\} = [A]^{-1}\{\delta_i, \delta_j\}^T. \tag{26}$$

By substituting the given values into Eq. (24), it is possible to derive the following expression:

$$\begin{Bmatrix} U(x,\theta) \\ W(x,\theta) \\ V(x,\theta) \end{Bmatrix} = [T][R][A]^{-1} \begin{Bmatrix} \delta_i \\ \delta_j \end{Bmatrix} = [N] \begin{Bmatrix} \delta_i \\ \delta_j \end{Bmatrix}. \tag{27}$$

The displacement function can be defined as:

$$[N] = [T][R][A]^{-1}. \tag{28}$$

2.6. Strain and stress vectors

The strain–displacement relationship for a conical shell can be derived from Eqs. (4) and (28), resulting in the strain tensor:

$$\{\varepsilon\} = \begin{bmatrix} [T] & [0] \\ [0] & [T] \end{bmatrix} [Q][A]^{-1} \begin{Bmatrix} \delta_i \\ \delta_j \end{Bmatrix} = [B] \begin{Bmatrix} \delta_i \\ \delta_j \end{Bmatrix}, \tag{29}$$

where $[Q]$ is a (6×8) matrix that can be found in Ref. [33]. Therefore, matrice $[B]$ is in the form of:

$$[B] = \begin{bmatrix} [T] & [0] \\ [0] & [T] \end{bmatrix} [Q][A]^{-1}. \tag{30}$$

2.7. Mass and stiffness matrices

The mass and stiffness matrices for each element of a conical shell based on the standard finite element method [56] are defined as follows:

$$[m_e] = \int_V \rho [N]^T [N] dV, \tag{31}$$

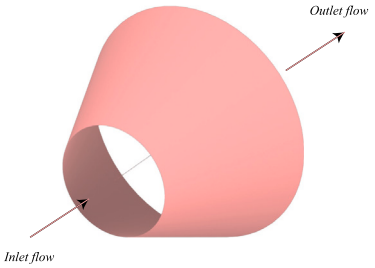

Fig. 4. Conical shell subjected to flowing fluid.

$$[k_e] = \int_V [B]^T [P][B] dV. \tag{32}$$

By substituting Eqs. (28) and (30) into Eqs. (31) and (32), respectively, and taking into account $dV = tx\sin(\alpha) d\theta dx$, followed by some mathematical manipulations, the final form of the mass and stiffness matrices for each element can be obtained:

$$\left[m_e\right] = \rho \int_{A_i} \left[A^{-1}\right]^T [R]^T [T]^T [T][R] \left[A^{-1}\right] x\sin(\alpha) h dx_i d\theta_i, \tag{33}$$

$$[k_e] = \int_{A_i} \left[A^{-1}\right]^T [Q]^T \begin{bmatrix} [T] & [0] \\ [0] & [T] \end{bmatrix}^T [P] \begin{bmatrix} [T] & [0] \\ [0] & [T] \end{bmatrix} [Q] \left[A^{-1}\right] x\sin(\alpha) h dx_i d\theta_i. \tag{34}$$

Here, ρ represent the material density. The global mass $\left[M_s\right]$ and stiffness matrices $\left[K_s\right]$ for the entire shell structure can be obtained by superimposing the mass $[m_e]$ and stiffness $[k_e]$ matrices for each finite element, using the standard assembling technique for different boundary conditions. The equations of motion for the shell are initially formulated in MAPLE and then implemented in Python code. With geometric and elastic property inputs, the Python code calculates the characteristic equation roots, shape functions, mass and stiffness matrices, and stress resultants for the structure.

3. Fluid modeling

Various mathematical models simulate the dynamics of stationary or flowing fluids. The nonlinear Navier–Stokes equations are the most accurate models as they account for viscosity, thermal dissipation, and body forces. However, due to their complexity, these equations are impractical for fluid–structure interaction (FSI) problems. Thus, simplifying assumptions are made to reduce complexity while maintaining accuracy. The commonly accepted assumptions for FSI problems are as follows [5]:

- Neglecting the effects of viscosity and body forces, as they increase complexity without significantly affecting accuracy.
- Assuming the fluid is purely irrotational.
- Considering the flow as adiabatic and isentropic, meaning no heat loss and reversible processes.
- Assuming fluid perturbation amplitudes are on the order of the shell thickness, justifying linear fluid vibration assumptions.
- Assuming the fluid pressure is perpendicular to the shell wall.
- Neglecting cavitation, ensuring continuous contact between the fluid and the shell walls.

These assumptions focus on primary fluid–structure interactions, minimizing computational errors. Consequently, our approach is efficient and applicable to specific engineering problems. For example, this approximation is suitable for analyzing large-scale offshore structures and aerospace components, where overall structural stability is the primary concern rather than detailed local fluid dynamics. In this study, the mathematical model uses linear potential flow to describe fluid behavior, assuming the fluid is inviscid, incompressible, and non-rotational. Additionally, the shell displacements are considered small enough for linear fluid mechanics to be applicable.

Fig. 4 shows the fluid–structure element. To ensure a valid model, the velocity potential function φ must satisfy the Laplace equation within the fluid domain expressed in the conical coordinate system [57].

$$\nabla^2\varphi = \frac{2}{x}\frac{\partial\varphi}{\partial x} + \frac{\partial^2\varphi}{\partial x^2} + \frac{1}{x^2(\sin\alpha)^2}\frac{\partial^2\varphi}{\partial\theta^2} + \frac{1}{x^2\tan\alpha}\frac{\partial\varphi}{\partial\alpha} + \frac{1}{x^2}\frac{\partial^2\varphi}{\partial\alpha^2}, \tag{35}$$

where x, θ, and α are the axial, circumferential, and coordinates along the semi-vertex angle of the conical shell, respectively.

The flow within the conical shell maintains a constant value across all its sections simultaneously. Consequently, for a specific conical shell, the product of the average fluid velocity is denoted as U_f, and the square of the x-coordinate remains uniform and is represented as Q_x at all points within the shell. This relationship can be expressed as:

$$Q_x = U_f . \pi R^2 = U . \pi x^2 \sin^2(\alpha), \tag{36}$$

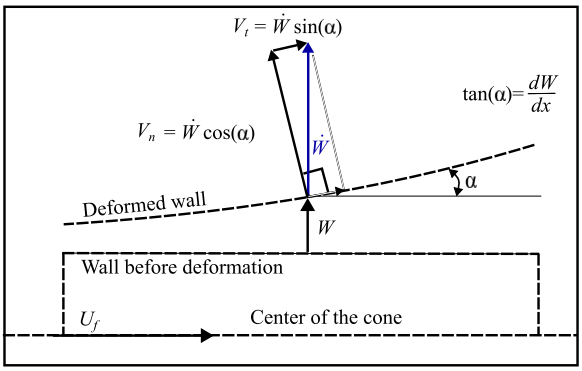

Fig. 5. Impermeability condition at the solid–fluid interface.

Q is considered as follows:

$$Q = \frac{Q_x}{\pi \sin^2(\alpha)}. \tag{37}$$

$$Q = U_f.x^2 = constant. \tag{38}$$

The velocity of the fluid can be represented as the gradient of the velocity potential function, given by [57]:

$$\mathbf{V} = \boldsymbol{\nabla}\varphi, \tag{39a}$$

$$V_x = \frac{Q}{x^2} + \frac{\partial\varphi}{\partial x}, \quad V_\theta = \frac{1}{x\sin\alpha}\frac{\partial\varphi}{\partial\theta}, \quad V_\alpha = \frac{1}{x}\frac{\partial\varphi}{\partial\alpha}, \tag{39b}$$

where V_x, V_θ, and V_α are the x, θ, and α components of the fluid velocity and Q/x^2 is the unperturbed flow velocity along the shell in the x-direction. The remaining components of velocity, V_x, V_θ, and V_α, are perturbation fluid velocities in three directions.

By employing the Bernoulli equation, the hydrodynamic pressure can be expressed in relation to the velocity potential as follows [35]:

$$p = -\rho_f \left[\frac{\partial\varphi}{\partial t} + \frac{Q}{x^2}\frac{\partial\varphi}{\partial x}\right]_{\zeta=a}, \tag{40}$$

where ρ_f represents the fluid density, ζ denotes the coordinate along the cone semi-vertex angle, and a is defined as follows, representing the half-angle of the inner wall opening of the shell:

$$\begin{cases} a = \alpha - \tan\left(\frac{t}{2x}\right), & \text{for internal fluid} \\ a = \alpha + \tan\left(\frac{t}{2x}\right), & \text{for external fluid.} \end{cases} \tag{41}$$

The impermeability condition ensures contact between the surface of the shell structure and the surrounding fluid. This condition requires the vertical component of the fluid's velocity to be equal to the rate of change of the shell's radial displacement, which is written as (see Fig. 5):

$$(V_\alpha)_{\alpha=a} = \frac{1}{x}\frac{\partial\varphi}{\partial\alpha}\bigg|_{\alpha=a} = \left[\dot{W} + \frac{Q}{x^2}W'\right]_{\zeta=a}. \tag{42}$$

Where W is the radial deflection of the shell. The technique of separating variables for solving the velocity potential is as follows:

$$\varphi(x,\theta,\alpha,t) = \sum_{q=1}^{8} R_q(\alpha)S_q(x,\theta,t), \tag{43}$$

where $R_q(\alpha)$ and $S_q(x,\theta,t)$ are the two separate functions to be determined. By using Eqs . (14) and (16), we have:

$$W(x,\theta,t) = \sum_{q=1}^{8} C_q y^{\lambda_q - 1}\cos n\theta e^{i\omega t} = \sum_{q=1}^{8} W_q, \quad y = \sqrt{x/l_e}. \tag{44}$$

The separate variable $S_q(x,\theta,t)$ is obtained by introducing Eq. (43) into Eq. (42):

$$S_q(x,\theta,t) = \frac{x}{R_q'(a)}\left[\dot{W} + \frac{Q}{x^2}W'\right]_{\alpha=a}. \tag{45}$$

Then, the velocity potential function can be expressed by substituting Eq. (45) into Eq. (43):

$$\varphi(x,\theta,\alpha,t)=\sum_{q=1}^{8} x\frac{R_q(\alpha)}{R_q'(a)}\left[\dot{W}+\frac{Q}{x^2}W'\right]_{\alpha=a}. \tag{46}$$

By substituting Eq. (46) into Eq. (43) and solving for a constant x, the following second-order differential equation in terms of R_q is obtained:

$$R_q''(\alpha)+\frac{1}{\tan\alpha}R_q'(\alpha)-\frac{n^2}{\sin^2\alpha}R_q(\alpha)=0. \tag{47}$$

In the case of internal flow, the truncated solution can be derived as follows:

$$R(\alpha)=C_1\cosh\left\{n\left[\log\left(\cos\left(\frac{\alpha}{2}\right)\right)-\log\left(\sin\left(\frac{\alpha}{2}\right)\right)\right]\right\}. \tag{48}$$

We define the Z parameter as follows:

$$Z=\frac{R(\alpha)}{R'(\alpha)}. \tag{49}$$

Upon substitution of Eqs. (48) and (49) into Eq. (46), the velocity potential function is derived. Utilizing Eq. (40), the total pressure exerted by the fluid onto the shell element can be calculated accordingly:

$$P_{\text{int}}=-\rho\sum_{j=1}^{8} xZ\left[\frac{\partial^2 W}{\partial^2 t}+\frac{2Q}{x^2}\frac{\partial^2 W}{\partial x\partial t}+\left(\frac{Q}{x^2}\right)^2\frac{\partial^2 W}{\partial^2 x}\right]. \tag{50}$$

By introducing Eq. (44) into Eq. (50), the final pressure relationship acting on the internal surface of the shell is deduced as follows:

$$\begin{aligned}P_{\text{int}}=&-\rho\sum_{j=1}^{8}\Bigg\{xZ[T]\left(\frac{x}{l_e}\right)^{\frac{(\lambda_j-1)}{2}}\ddot{C}\\&+Z[T]\left(\frac{Q}{x^2}\right)(\lambda_j-1)\left(\frac{x}{l_e}\right)^{\frac{(\lambda_j-1)}{2}}\dot{C}\\&+Z[T]\left(\frac{Q^2}{4x^5}\right)(\lambda_j-1)(\lambda_j-3)\left(\frac{x}{l_e}\right)^{\frac{(\lambda_j-1)}{2}}C\Bigg\}.\end{aligned} \tag{51}$$

The equation is simplified by defining the following matrices and performing mathematical manipulations.

$$\left[R_{f1}\right]=\begin{bmatrix}0&\cdots&0\\ r_{f1}(2,1)&\cdots&r_{f1}(2,8)\\ 0&\cdots&0\end{bmatrix}_{3\times8}\begin{bmatrix}Z&\cdots&0\\ \vdots&\ddots&\vdots\\ 0&\cdots&Z\end{bmatrix}_{8\times8}, \tag{52}$$

where r_{f1} is defined as:

$$r_{f1}(2,j)=\left(\frac{x}{l_e}\right)^{\frac{(\lambda_j-1)}{2}},\ j=1,\ldots,8. \tag{53}$$

Similarly, introducing $\left[R_{f2}\right]$ and $\left[R_{f3}\right]$ as follows:

$$\left[R_{f2}\right]=\begin{bmatrix}0&\cdots&0\\ r_{f2}(2,1)&\cdots&r_{f2}(2,8)\\ 0&\cdots&0\end{bmatrix}_{3\times8}\begin{bmatrix}Z&\cdots&0\\ \vdots&\ddots&\vdots\\ 0&\cdots&Z\end{bmatrix}_{8\times8}, \tag{54}$$

where r_{f2} is as:

$$r_{f2}(2,j)=\left(\frac{x}{l_e}\right)^{\frac{(\lambda_j-1)}{2}}(\lambda_j-1),\quad j=1,\ldots,8, \tag{55}$$

and

$$\left[R_{f3}\right]=\begin{bmatrix}0&\cdots&0\\ r_{f3}(2,1)&\cdots&r_{f3}(2,8)\\ 0&\cdots&0\end{bmatrix}_{3\times8}\begin{bmatrix}Z&\cdots&0\\ \vdots&\ddots&\vdots\\ 0&\cdots&Z\end{bmatrix}_{8\times8}, \tag{56}$$

and r_{f3} is defined as:

$$r_{f3}(2,j)=\left(\frac{x}{l_e}\right)^{\frac{(\lambda_j-1)}{2}}(\lambda_j-1)(\lambda_j-3),\quad j=1,\ldots,8. \tag{57}$$

Finally, the simplified equation for the total pressure, as applied to each individual element, is presented as follows:

$$P_{\text{int}} = -\rho \left\{ x[T]\left[R_{f1}\right][A]^{-1}\{\ddot{\delta}\} + \left(\frac{Q}{x^2}\right)[T]\left[R_{f2}\right][A]^{-1}\{\dot{\delta}\} + \left(\frac{Q^2}{4x^5}\right)[T]\left[R_{f3}\right][A]^{-1}\{\delta\} \right\}. \tag{58}$$

The shape function for fluid elements is introduced in the following manner:

$$\left[N_{fi}\right] = [T]\left[R_{fi}\right][A]^{-1}, i = 1, 2, 3. \tag{59}$$

The general force vector exerted by the fluid on the structure can be determined through integration by employing the following equation:

$$\{F\}_{\text{e}} = \int_A [N]^{\text{T}}\{P\}\text{d}A. \tag{60}$$

Where $[N]$ represents the shape function matrix of the finite element as defined in Eq. (28) for the structural component, $\{P\}$ is a vector representing the fluid pressure exerted on the structural element, and $dA = x\sin(\alpha)d\theta dx$ is the interface area between the fluid and the structure. The force vector can be obtained by substituting the shape function from Eq. (28) and the pressure from Eq. (58) into Eq. (60), resulting in the determination of the mass, damping, and stiffness matrices for the flowing fluid. These matrices are evaluated through the computation of the matrix operation required by the finite element method, as provided by the following equation:

$$\left[m_f\right] = -\rho \int x[N]^T \left[N_{f1}\right] dA, \tag{61a}$$

$$\left[c_f\right] = -\rho Q \int \frac{1}{x^2}[N]^T \left[N_{f2}\right] dA, \tag{61b}$$

$$\left[k_f\right] = -\frac{\rho Q^2}{4} \int \frac{1}{x^5}[N]^T \left[N_{f2}\right] dA. \tag{61c}$$

These matrices represent the influence of inertia, Coriolis, and centrifugal effects on an element. In particular, the Coriolis force, represented as $\left[c_f\right]$, emerges as a consequence of the interaction between the relative velocity of the fluid and the rotation of a segment of the structure. The centrifugal and Coriolis terms introduce non-conservative components into the present problems. Mathematically, these terms give rise to differential equations that lead to complex eigenvalue problems. Physically, these effects can result in both static and dynamic instabilities within the system.

4. Eigenvalue and eigenvector problem

The dynamic response of a shell is influenced by the presence of fluid, which applies pressure to the structure and can be modeled as a function of displacement, velocity, and acceleration. These three components represent the stiffness, Coriolis, and inertial effects of the fluid forces. The dynamic equations of a coupled fluid–structure system can be formed by combining the fluid force matrices with the structural matrices. The following equation describes the general dynamic response of this system:

$$\left(\left[M_s\right] + \left[M_f\right]\right)\left\{\ddot{\delta}_T\right\} + \left[C_f\right]\left\{\dot{\delta}_T\right\} + \left(\left[K_s\right] + \left[K_f\right]\right)\left\{\delta_T\right\} = \{F\}, \tag{62}$$

The symbol s represents the shell without fluid, and f represents the fluid. In this context, the inertial, Coriolis, and centrifugal forces arising from potential flow are characterized as $\left[M_f\right]$, $\left[C_f\right]$, and $\left[K_f\right]$, respectively. These forces affect the vibration pattern and are coupled with the elastic deformation of the conical shell. In this case, the vector $\{F\}$ represents external forces applied to the system, which can be considered negligible. When the fluid remains stationary, the terms associated with fluid velocity become negligible, simplifying the global equations of motion. It is essential to note that this analysis focuses on linear theory and does not consider the nonlinear coupling between low-frequency free surface modes and shell modes. Additionally, structural damping is not taken into account due to its insignificance compared to inertia for thin shells in this study.

The mass and stiffness matrices, each with dimensions $N_d(N_e + 1)$, are typically square and symmetric, where N_e is the number of elements, and N_d represents the number of degrees of freedom at each node. In this case, $N_d = 4$. Boundary conditions are considered by removing specific rows and columns from the total mass, stiffness, and damping matrices of the shell. Nodal boundary conditions are outlined in Table 1, where "initial" and "final" nodes correspond to the small and large edges of the truncated cone. For example, the notation "*C-F*" signifies a clamped boundary condition at the small edge and a free boundary condition at the large edge. After applying the boundary conditions, the global matrices are reduced to square matrices of order $4(N_e + 1) - N_c$, where N_c is the number of applied constraints.

The equations governing the free response of a system with general damping cannot be decoupled using principal coordinates. Instead, the state-space method [58] transforms the system into a set of $2n$ first-order differential equations, where n represents the degrees of freedom. These equations involve the generalized coordinates and their first derivatives. When Lagrange's equations are applied to a system with viscous damping, it leads to n second-order differential equations in terms of the generalized coordinates x.

$$\mathbf{M}\ddot{\mathbf{x}} + \mathbf{C}\dot{\mathbf{x}} + \mathbf{K}\mathbf{x} = 0, \tag{63}$$

Table 1
Naming convention for boundary conditions.

Boundary condition	Edge Constraint	node i[a]	node j[a]
Clamped (C)	$U = W = \frac{\partial W}{\partial x} = V = 0$	1, 2, 3, 4	$(4N+1), (4N+2), (4N+3), (4N+4)$
Simply Supported (SS)	$V = W = 0$	2, 4	$(4N+2), (4N+4)$
Free (F)	No Constraint	None	None

[a] Rows and columns deleted.

where

$$[M] = [M_s] + [M_f]$$
$$[C] = [C_f] \tag{64}$$
$$[K] = [K_s] + [K_f]$$

The hydroelastic instability conditions of the shell are determined by calculating the eigenvalues of Eq. (63). In order to rewrite Eq. (63) in terms of $\mathbf{y}_1$ and $\mathbf{y}_2$, vectors $\mathbf{y}_1 = \mathbf{x}$ and $\mathbf{y}_2 = \dot{\mathbf{x}}$ are defined.

$$\begin{bmatrix} \dot{\mathbf{y}}_1 \\ - \\ \dot{\mathbf{y}}_2 \end{bmatrix} = \begin{bmatrix} 0 & | & \mathbf{I} \\ - & | & - \\ -\mathbf{M}^{-1}\mathbf{K} & | & -\mathbf{M}^{-1}\mathbf{C} \end{bmatrix} \begin{bmatrix} \mathbf{y}_1 \\ - \\ \mathbf{y}_2 \end{bmatrix} \tag{65}$$

The eigenvalue problem is given by:

$$|[DD] - \Lambda[I]| = 0, \tag{66}$$

where $[DD]$ is defined as:

$$[DD] = \begin{bmatrix} 0 & | & \mathbf{I} \\ - & | & - \\ -\mathbf{M}^{-1}\mathbf{K} & | & -\mathbf{M}^{-1}\mathbf{C} \end{bmatrix} \tag{67}$$

Eigenvalues obtained can be expressed in dimensionless parameters as introduced in Ref. [34]:

$$\Omega = \omega R_2 \sqrt{\rho\left(1 - v^2\right)/E} \tag{68}$$

where, Ω is the natural frequency, R_2 is the large end radius of the shell.

5. Numerical results and discussions

5.1. Validation

In this study, a Python-based computational tool was developed to analyze the stability of conical shells with ring-stiffeners exposed to flowing fluid. The previous study by the authors [18] performed comparative analyses to validate the method proposed in this study, focusing on empty and fluid-filled shells. The following sections investigate the validation and impact of parameters such as boundary conditions, cone semi-vertex angles, and the number of rings on the critical flow discharge of the shells. To verify the accuracy of the model with ring-stiffeners, calculations were conducted on an empty conical shell with ring-stiffeners. The results were compared against the theoretical predictions and experimental measurements from Weingarten's study [11]. The conical shell geometry includes a thickness of 0.06 in and a semi-vertex angle of 20°. The shell has small and large radii of 1.21 in and 3.03 in, respectively. The material properties are defined by a Young's modulus (E) of 10^7 lb/in^2, a Poisson's ratio (v) of 0.3, and a density (ρ) of 2.54×10^{-4} lbs^2/in^4, with *C-C* boundary conditions. The shell is reinforced with eleven external ribs, each having a height of 0.095 in, a width of 0.125 in, and spaced at a pitch of 0.50 in. As described in Section 2.3, the shell is divided into 23 finite elements, representing either stiffened or unstiffened sections. The results, presented in Table 2, closely align with the experimental data, with the maximum error observed at $m = 1$ and $n = 2$.

Kumar and Ganesan [34] investigated the dynamics of fluid-conveying unstiffened conical shells with specific geometries, including a conical shell made of mild steel with a middle radius of 0.876 m, a length of 0.9144 m, and a thickness of 1.5 mm. The study examined shells with semi-vertex angles of 10°, 30°, and 60° under various boundary conditions (*C-C*, *SS-SS*, and *C-F*). To validate their model, the variation in dimensionless frequency with flow discharge for selected circumferential modes was analyzed, as shown in Fig. 6. They also conducted repeated analyses for circumferential mode numbers two to fifteen, determining critical velocities for each mode number. The study aimed to identify correlations between circumferential buckling modes of fluid-conveying shells and the mode with the lowest natural frequency. Our model was validated by comparing the critical velocities under *C-F* boundary conditions for a cone with a semi-vertex angle of 30°. The critical velocity was calculated by dividing the cone's critical discharge (Q_x) by its middle cross-sectional area. Table 3 confirms the consistency between the results of the current model and those from Kumar and Ganesan's findings.

Table 2
Comparison of natural frequencies of ring stiffened conical shell obtained by Weingarten theoretical and experimental work [11] with those of present method.

n	m=1 (kHz)			m=2 (kHz)			m=3 (kHz)		
	Theo.	Exp.	Present	Theory	Exp.	Present	Theory	Exp.	Present
2	4.004	2.570	4.155	7.818	6.761	7.480	10.319	10.278	10.126
3	3.552	3.134	3.661	6.641	5.267	6.129	9.104	8.441	8.810
4	4.792	4.492	4.618	7.430	6.522	6.759	9.253	9.213	9.116
5	6.414	6.079	6.137	8.804	8.093	8.471	10.428	10.537	10.909
6	8.454	8.037	8.053	10.841	10.453	10.704	12.743	12.778	13.419
7	10.717	10.341	10.312	13.398	12.884	13.336	15.789	15.899	16.376
8	13.433	12.869	12.878	16.773	15.829	16.304	20.120	18.692	19.693
9	16.943	–	15.726	20.345	–	19.573	–	–	23.324
10	20.493	–	18.839	–	–	23.121	–	–	27.242

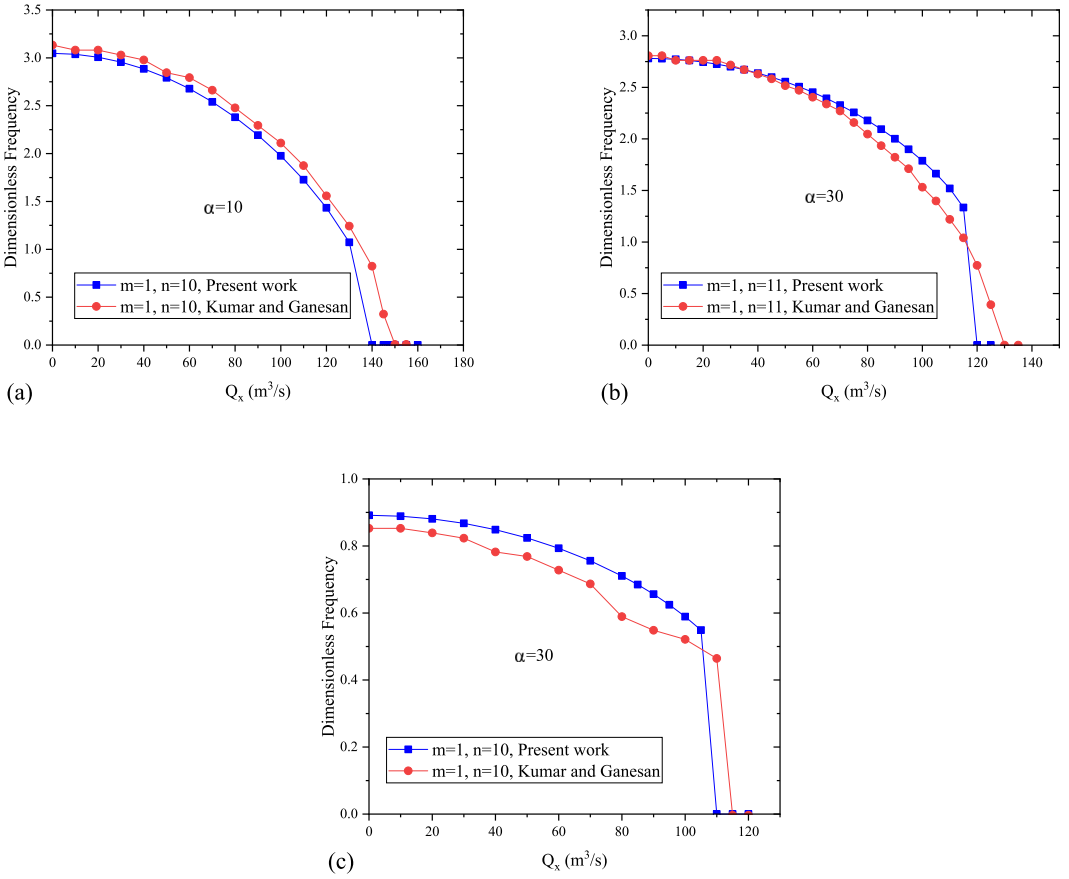

Fig. 6. Comparison of the dimensionless frequency with respect to flow discharge (Q) for water flowing through the conical shell under (a) *SS-SS*, (b) *C-C*, and (c) *C-F* boundary conditions [34].

5.2. Static divergence studies on ring-stiffened conical shells

This study aims to predict the onset of instability in ring-stiffened shells subject to flowing fluid, focusing on the relationship between critical flow discharge and the natural frequency characteristics of fluid-conveying conical shells. Additionally, the study evaluates the effects of ring stiffeners and shell geometry on critical velocity and the initiation of divergence. The findings indicate that an increase in flow discharge leads to a decrease in the imaginary part of eigenvalues, reaching zero at the critical discharge point, which suggests divergence-type instability. In structural engineering, buckling is recognized as a mode-specific instability influenced by mechanical, geometric, and material parameters. This study concentrates on the stability loss of the divergence type. To elucidate the types of instabilities, a detailed examination of both the real and imaginary parts of eigenvalues, as suggested in Ref. [31], is necessary. They suggests that an increase in the cone angle might alter the form of instability from divergence to flutter in conical shells. The conical shell analyzed in this study features a semi-vertex angle of 30°, a large end radius (R_2) of 1.14 m, and

Table 3
Comparison of critical velocity of different circumferential mode numbers of a conical shell conveying fluid under *C-F* condition.

Boundary condition	Circumferential mode numbers	Critical velocity (m/s)	
		Present work	Kumar and Ganesan [34]
C-F	5	49.776	45.190
	6	41.554	35.837
	7	36.332	32.700
	8	39.480	34.128
	9	42.554	39.898
	10	46.628	48.159
	11	48.702	50.680
	12	50.776	54.741
	13	56.998	58.017
	14	57.998	60.510
	15	59.072	63.927

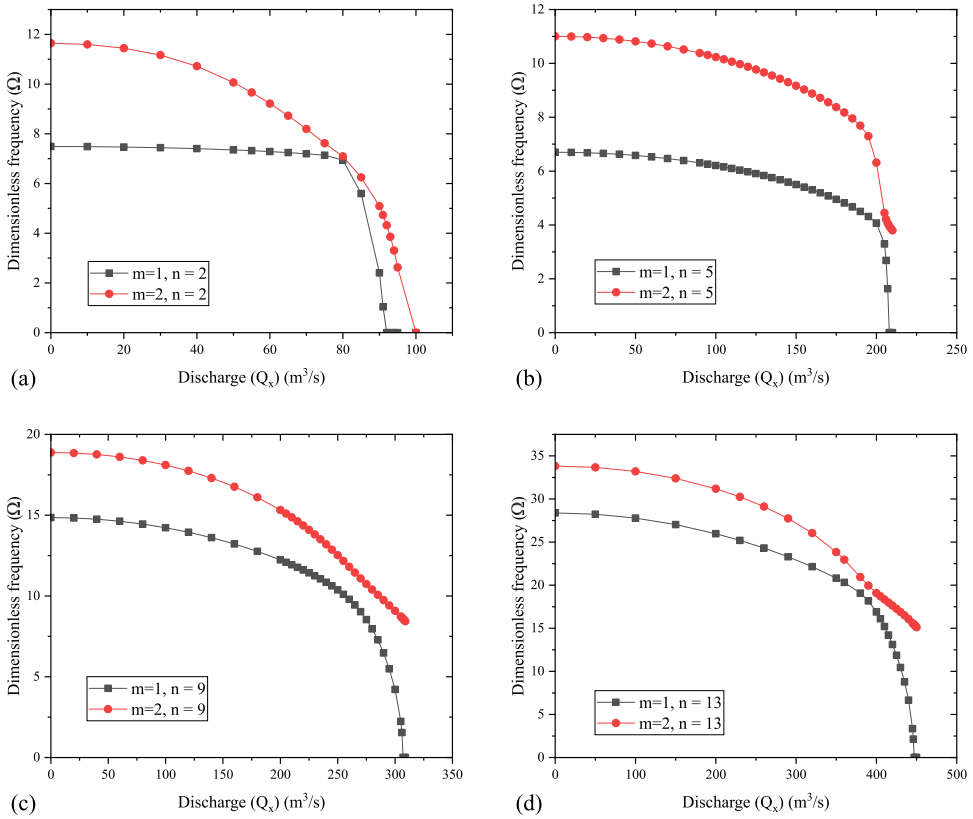

Fig. 7. Variation of dimensionless frequency with respect to discharge (Q_x) for water flowing through the conical shell of semi-vertex angle $\alpha = 30$ with number of rings = 9, $n = 2, 5, 9, 13$, with *C-C* boundary condition.

a radius ratio (R_2/R_1) of 1.863, set under *C-C* boundary conditions. The shell, with a constant thickness of 1.5 mm, includes nine equally spaced ring stiffeners, each with a rectangular cross-section measuring 0.01 m in width and 0.02 m in height. The material properties are defined with a Young's modulus (E) of 2×10^{11} N/m^2, a Poisson's ratio (ν) of 0.3, and a density (ρ) of 7800 kg/m^3, while the fluid within the shell has a density of $\rho = 1000$ kg/m^3. The analysis includes fifteen circumferential modes (n = 2–15) and corresponding axial modes ($m = 1, 2$). Fig. 7 depicts the variation of flow discharge (Q) with dimensionless frequency (Ω) for different circumferential and axial mode numbers. The detailed analysis for each circumferential mode number is not reported here for the sake of brevity. Variations of the dimensionless frequency versus the fluid velocity are obtained for each boundary condition, at a specific circumferential wave number and semi-vertex angle, using sufficiently small velocity increments. Critical

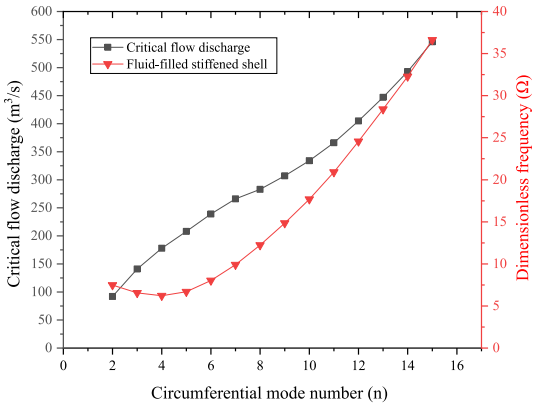

Fig. 8. Dimensionless frequencies (Ω) and critical flow discharge (m^3/s) of a ring-stiffened conical shell for $\alpha = 30$ with *C-C* boundary conditions, $m = 1$.

Table 4
Comparison of critical flow discharge and dimensionless frequency of different circumferential mode numbers of a conical shell conveying fluid with and without ring-stiffeners under *C-C* condition, $\alpha = 30$.

Boundary condition	Circumferential mode numbers	Critical flow discharge. (m^3/s)		Dimensionless frequency (Ω)	
		Ring-stiffened shell	Unstiffened shell [34]	Ring-stiffened shell	Unstiffened shell [34]
C-C	7	266	165	9.903	3.427
	8	283	147	12.232	3.107
	9	307	135	14.851	2.886
	10	334	129	17.687	2.773
	11	366	126	20.908	2.771
	12	405	132	24.568	2.877

fluid velocities are then identified across different wave numbers. The minimum fluid velocity where at least one imaginary part of the frequency is zero is considered as the critical velocity for that specific circumferential wave number and semi-vertex angle. It should be noted that critical velocities occur at significant intervals, and if the velocity increments are not sufficiently small, some instability modes may not be detected. Fig. 8 demonstrates the critical flow discharge for various circumferential modes and the first axial mode of a fluid-conveying stiffened shell. It is observed that as the number of circumferential waves increases, the critical velocity also increases. Conversely, for fluid-filled stiffened shells, the dimensionless frequency initially decreases and then increases. The former is attributed to the sensitivity of instability modes to the conical shell stiffness, where the mode with the lowest frequency is more likely to lose stability first due to lower stiffness. According to the study, the circumferential mode number with the lowest critical discharge is two, while the mode with the lowest dimensionless frequency is four. Additional investigations involving various boundary conditions, such as *C-F* and *SS-SS*, are explored in subsequent sections.

5.3. Effect of boundary conditions on the instability of ring-stiffened conical shells

A similar investigation was conducted to examine the effect of flowing fluid on the critical flow discharge under *SS-SS* and *C-F* boundary conditions. The variation of the dimensionless frequency with flow discharge for certain circumferential mode numbers is depicted in Figs. 9 and 10 for *SS-SS* and *C-F* boundary conditions, respectively. The results indicate that similar to the *C-C* boundary condition, the imaginary part of eigenvalues decreases with increasing flow discharge and reaches zero at the critical flow discharge. Additionally, the critical flow discharge increases as the number of circumferential waves increases, as shown in Fig. 11. This trend is also observed for stiffened shells filled with quiescent fluid, where the dimensionless frequency first decreases and then increases as the circumferential mode increases. Based on the critical flow discharge data presented in Tables 4 to 6, it is evident that the critical flow discharge increases for each successive circumferential mode compared to an unstiffened shell. The dimensionless frequency of a fluid-filled stiffened shell is observed to be higher than that of an unstiffened shell due to the increased stiffness of the ring stiffeners across all boundary conditions. Fig. 12 illustrates the impact of different boundary conditions on the critical flow discharge (m^3/s) and dimensionless frequency of a fluid-filled, ring-stiffened conical shell. The graph shows that the dimensionless frequency of the *C-C* boundary condition is higher than that of the other boundary conditions. It is also observed that for each circumferential mode number, the stiffened shell with a *C-C* boundary condition has a higher value of critical flow discharge, indicating that instability of the specific circumferential mode number is more likely to occur first in a *SS-SS* condition due to the lower stiffness of the shell in this condition compared to *C-F* and *C-C* boundary conditions.

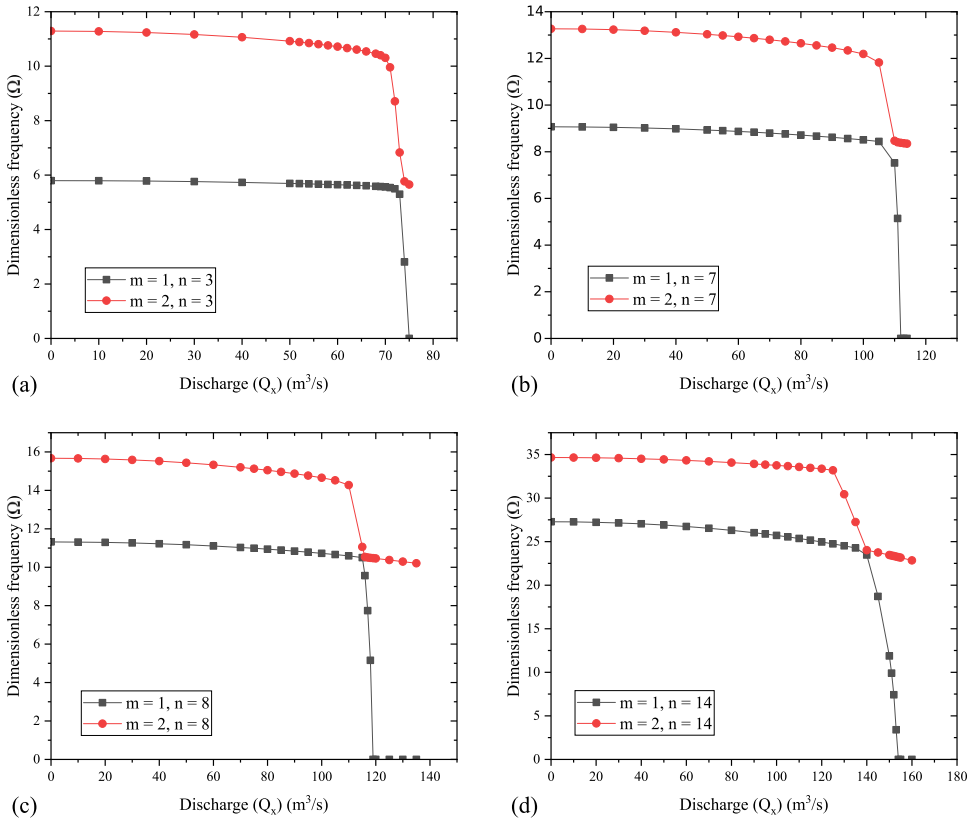

Fig. 9. Variation of the dimensionless frequency with respect to discharge (Q_x) for water flowing through the conical shell of vertex angle $\alpha = 30$ with the number of rings = 9, $n = 3, 7, 8, 14$, for *SS-SS* boundary condition.

Table 5
Comparison of critical flow discharge and dimensionless frequency of different circumferential mode numbers of a conical shell conveying fluid with and without ring-stiffeners under *SS-SS* boundary condition, $\alpha = 30$.

Boundary condition	Circumferential mode numbers	Critical flow discharge. (m^3/s)		Dimensionless frequency (Ω)	
		Ring-stiffened shell	Unstiffened shell [34]	Ring-stiffened shell	Unstiffened shell [34]
SS-SS	7	114	110	9.068	2.231
	8	119	98	11.315	1.976
	9	126	90	13.904	1.872
	10	132	94	16.563	1.906
	11	137	102	19.433	2.055
	12	143	111	22.413	2.288

Table 6
Comparison of critical flow discharge and dimensionless frequency of different circumferential mode numbers of a conical shell conveying fluid with and without ring-stiffeners under *C-F* condition, $\alpha = 30$.

Boundary condition	Circumferential mode numbers	Critical flow discharge. (m^3/s)		Dimensionless frequency (Ω)	
		Ring-stiffened shell	Unstiffened shell [34]	Ring-stiffened shell	Unstiffened shell
C-F	7	193	78	5.088	0.609
	8	195	82	6.060	0.642
	9	193	94	6.849	0.743
	10	190	116	7.496	0.894
	11	190	122	7.908	1.0821
	12	191	131	8.251	1.300

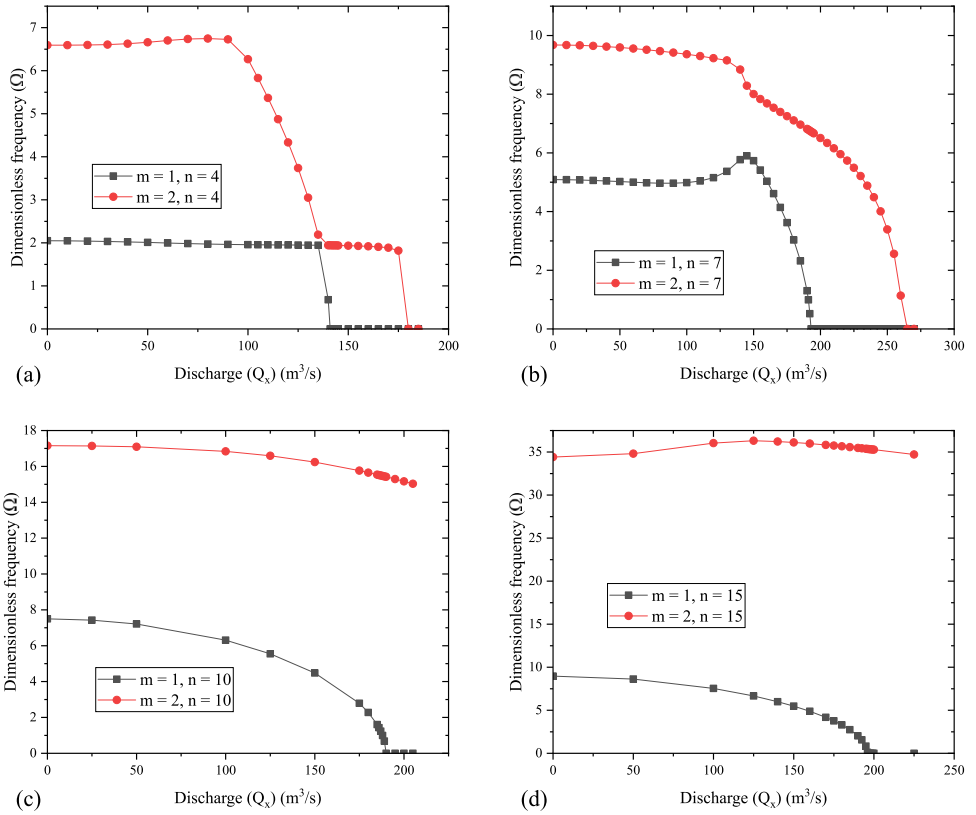

Fig. 10. Variation of dimensionless frequency with respect to discharge (Q_x) for water flowing through the conical shell of vertex angle $\alpha = 30$ with number of rings = 9, $n = 4, 7, 10, 15$, for *C-F* boundary condition.

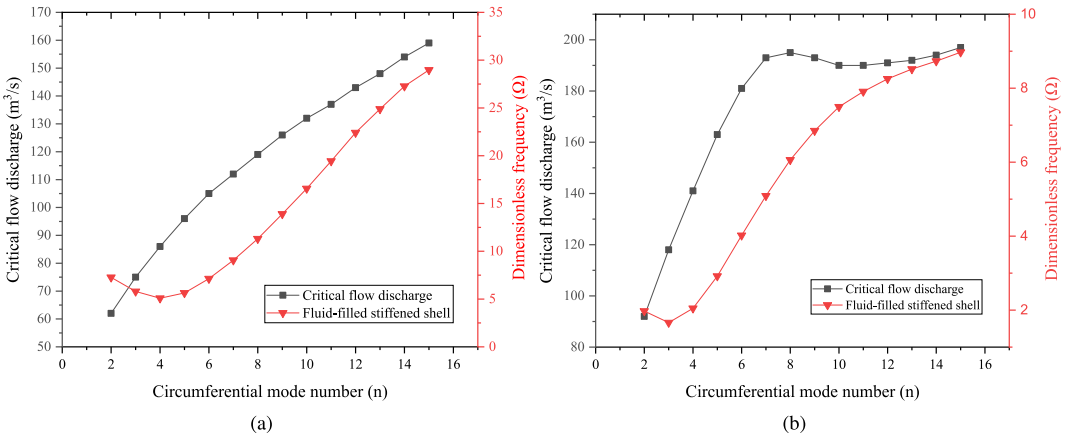

Fig. 11. Dimensionless frequencies (Ω) and critical flow discharge (m^3/s) of a ring-stiffened conical shell for $\alpha = 30$ with (a) *SS-SS*, (b) *C-F* boundary conditions; $m = 1$.

5.4. Effect of number of rings stiffeners on the instability of conical shells

The relationship between the number of rings and critical flow discharge requires comprehensive analysis through analytical studies for a precise understanding. Figs. 13–15 illustrate the impact of the number of stiffeners on the critical flow discharge and dimensionless frequency of the shell under different boundary conditions. Contrary to expectations, an increase in the number of rings does not consistently raise the critical flow discharge, revealing a dependency on boundary conditions. The unexpected

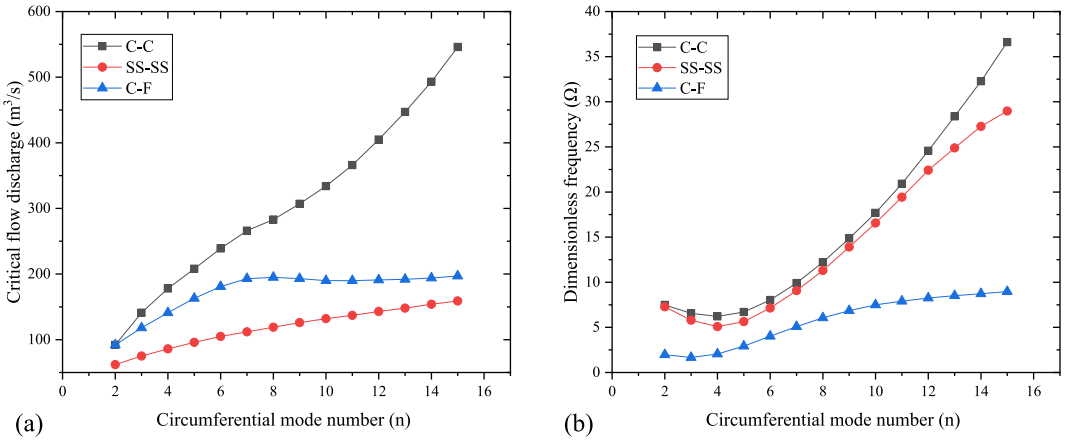

Fig. 12. Critical flow discharge (m^3/s) and dimensionless frequencies (Ω) of ring-stiffened conical shell for $\alpha = 30$, and different boundary conditions, $m = 1$.

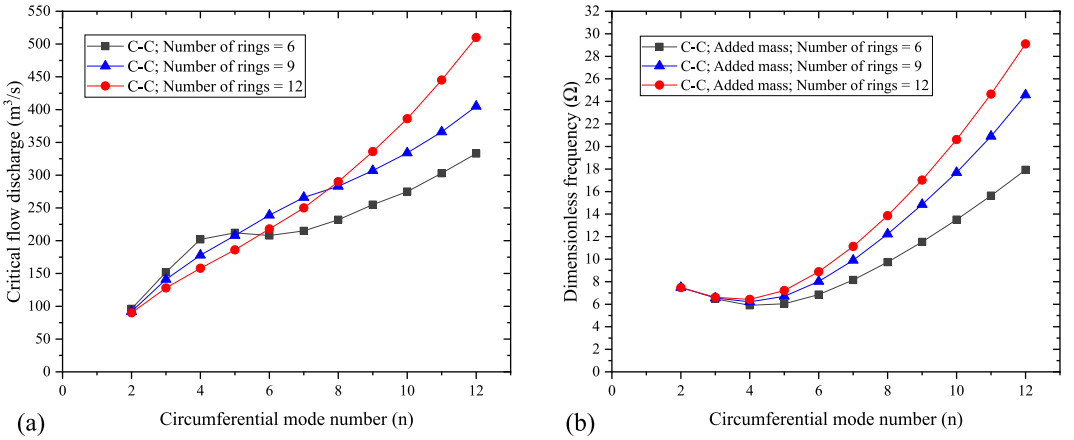

Fig. 13. Effect of the number of ring stiffeners on critical flow discharge (m^3/s) and dimensionless frequencies (Ω) of conical shells with $\alpha = 30$ under *C-C* boundary conditions, $m = 1$.

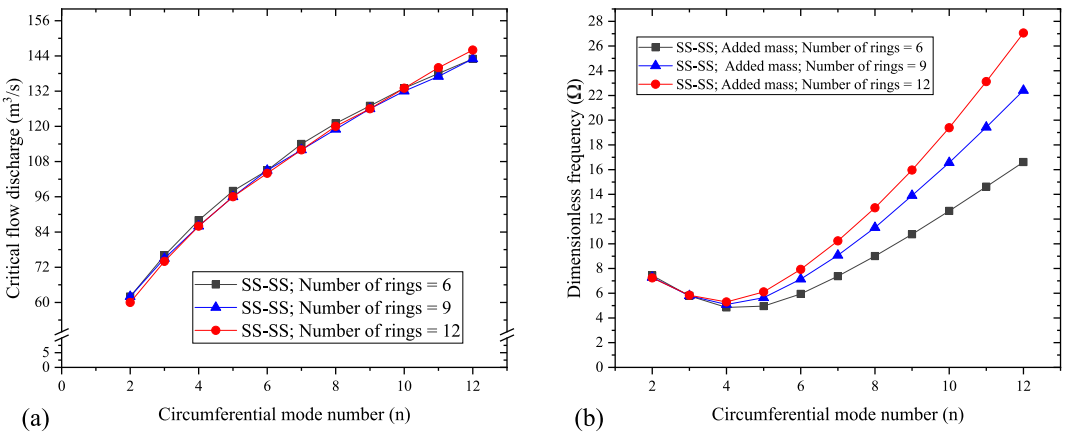

Fig. 14. Effect of the number of ring stiffeners on critical flow discharge (m^3/s) and dimensionless frequencies (Ω) of conical shells with $\alpha = 30$ under *SS-SS* boundary conditions, $m = 1$.

variation in critical velocity for different numbers of rings might be attributed to the complex interplay between structural rigidity, fluid dynamics, and specific boundary constraints.

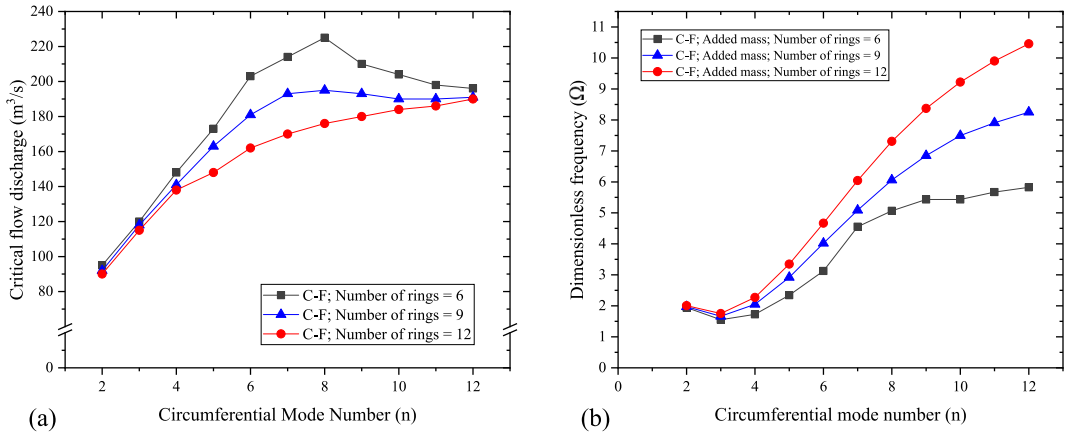

Fig. 15. Effect of the number of ring stiffeners on critical flow discharge (m^3/s) and dimensionless frequencies (Ω) of conical shells with $\alpha = 30$ under *C-F* boundary conditions, $m = 1$.

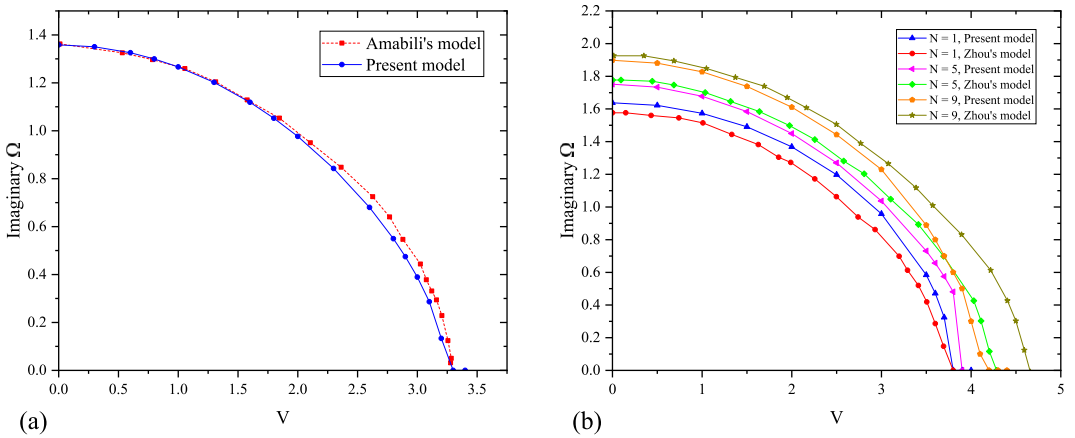

Fig. 16. Comparison of the first (m = 1) nondimensional eigenvalues between the present model and (a) Amabili's model [59] for n = 5 in a *SS-SS* unstiffened cylindrical shell, and (b) Zhou's model [60] for n = 4 for different numbers of stiffeners, both as a function of nondimensional fluid velocity *V*.

- Under a *SS-SS* boundary condition, the number of rings has the least effect on the critical flow discharge for the given shell and ring geometry. However, increasing in the number of rings leads to a rise in the dimensionless frequency for fluid-filled ring-stiffened shells across all circumferential mode numbers. The minimal effect of the number of rings on critical flow discharge in *SS-SS* conditions may be due to the dominance of the structural constraints imposed by the support type, overshadowing the impact of additional rings.
- For a *C-F* boundary condition, increasing in the number of rings results in a decrease in critical flow discharge, particularly for circumferential mode numbers higher than four. The structural constraints at the smaller end may influence the overall instability behavior of the shell. With six equally spaced rings, the shell may exhibit increased stability due to the distributed support, resulting in a higher critical velocity. However, as the number of rings increases, the effect of the added structural support may alter the overall flexibility, potentially leading to a lower critical velocity. Conversely, there is an increase in the dimensionless frequency of the added mass with an increase in the number of rings.
- In the case of a *C-C* boundary condition, the behavior of the number of rings in the critical flow discharge of the stiffened shell is unpredictable. Increasing in the number of rings raises the critical flow discharge for circumferential mode numbers higher than eight. However, for mode numbers lower than eight, shells with fewer rings have a higher critical flow discharge. An increase in the number of rings leads to an increase in the dimensionless frequency of a stiffened shell fully filled with water.

A more detailed analysis was conducted to validate the current model's ability to capture the effect of rings on the critical fluid velocity. The analysis focused on the critical fluid velocity of a ring-stiffened cylindrical shell. Zhou [60] validated his model for an unstiffened cylindrical shell against Amabili's results [59]. He then extended his study to consider how the number of ring stiffeners influences the natural frequency and critical fluid velocity. Zhou concluded that an increase in the number of rings results in a

Table 7
Comparison of critical velocity of fundamental circumferential mode numbers of a cylindrical shell conveying fluid under *SS-SS* boundary condition.

N_r (Number of rings)	Fundamental circumferential mode numbers	Critical velocity (m/s)		
		Present model	Zhou's model [60]	Amabili's model [59]
1	4	3.8	3.8	–
5	4	3.9	4.3	–
9	4	4.2	4.7	–
Unstiffened shell	5	3.3	3.3	3.3

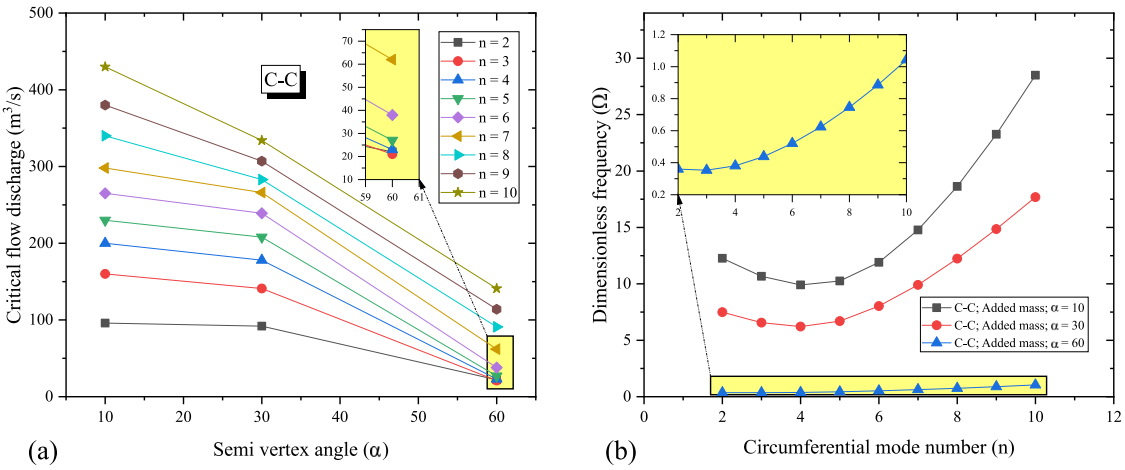

Fig. 17. Effect of cone's semi-vertex angle on critical flow discharge (m^3/s) and dimensionless frequencies (Ω) of ring-stiffened conical shells with $\alpha = 30$ under *C-C* boundary conditions, $m = 1$.

higher natural frequency and critical fluid velocity. The present model, illustrated in Fig. 16, aligns with Amabili's results for an unstiffened cylindrical shell. Subsequent analysis, using the same configuration, explores the impact of the number of rings. Fig. 16 and Table 7 show that the current model produces satisfactory results across the velocity range, consistent with Zhou's findings, and agrees with critical flow discharge outcomes for the fundamental mode number, as compared to results obtained by Amabili and Zhou. Discrepancies may arise from the use of different theories; Zhou utilized a smeared method to account for ring stiffeners, while the present method employed a discretized approach. Additionally, Zhou's results are digitized, introducing inherent differences. It is worth noting that Amabili's model was based on the fundamental mode $n = 5$, while Zhou's model considered the fundamental mode $n = 4$. This study encompasses all circumferential mode numbers ($n = 2 - 10$), obtaining the critical fluid velocity for each circumferential mode number. The geometry, definition of dimensionless velocity, and imaginary part of eigenvalues can be found in Ref. [60]. Therefore, the current model suggests that increasing the number of rings can enhance the critical fluid velocity and natural frequency, similar to cylindrical shells. However, this trend is different for conical shells. In conical shells, increasing the number of rings results in a higher natural frequency of the fluid-filled shell ($U_f = 0$) due to increased stiffness. However, the critical fluid velocity in conical shells does not always increase with the number of rings. Instead, it is influenced by factors such as boundary conditions, the number of circumferential modes, and the semi-vertex angle of the cone.

5.5. *Effect of semi-vertex angles on the instability of ring-stiffened conical shells*

In this section, we present the results of studying the effect of the semi-vertex angle on the critical flow discharge of the ring-stiffened conical shell under the influence of flowing fluid, as well as the dimensionless frequency of the shell when filled with stationary fluid. The key observations obtained from Figs. 17–19 are as follows:

- For *C-C* and *SS-SS* boundary conditions, an increase in the semi-vertex angle (α) leads to a consistent decrease in the critical flow discharge at which static divergence occurs. This trend is observed for all circumferential mode numbers.
- For *C-F* boundary conditions, a distinct behavior is observed. For $\alpha = 10$, the critical flow discharge is lower compared to $\alpha = 30$ and higher than $\alpha = 60$, regardless of the circumferential mode numbers.
- Across all boundary conditions, an increase in the semi-vertex angle results in a decrease in the dimensionless frequency of the fluid-filled conical shell. This behavior can be attributed to the reduced stiffness of the shell as the semi-vertex angle increases.

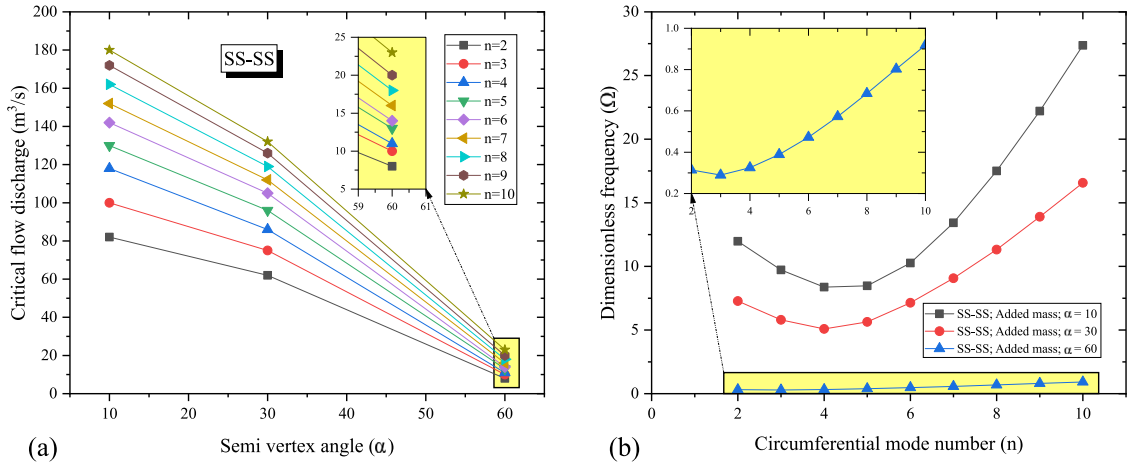

Fig. 18. Effect of cone's semi-vertex angle on critical flow discharge (m^3/s) and dimensionless frequencies (Ω) of ring-stiffened conical shells with $\alpha = 30$ under *SS-SS* boundary conditions at both ends, $m = 1$.

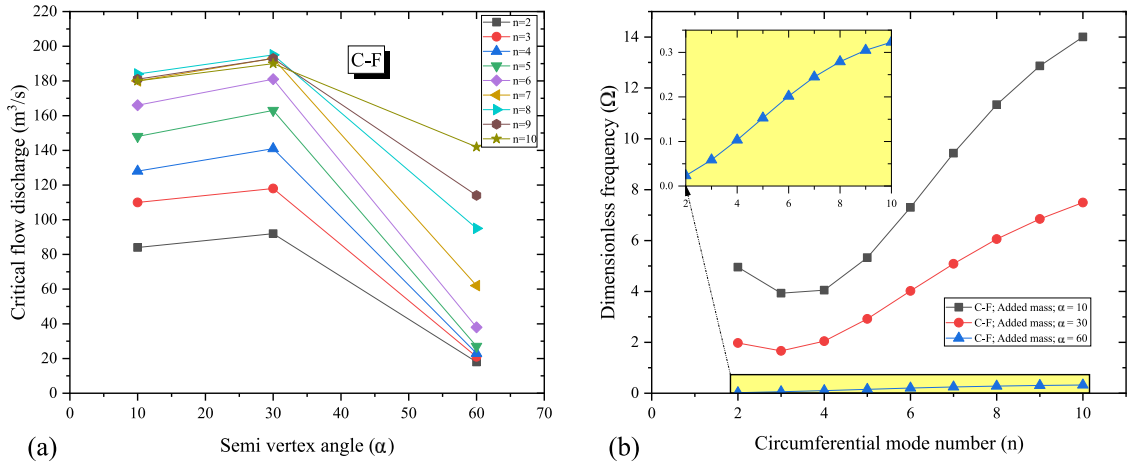

Fig. 19. Effect of cone's semi-vertex angle on critical flow discharge (m^3/s) and dimensionless frequencies (Ω) of ring-stiffened conical shells with $\alpha = 30$ under *C-F* boundary conditions, $m = 1$.

6. Conclusion

The present model used a hybrid approach to predict the dynamic behavior and stability analysis of truncated conical shells with ring stiffeners conveying fluid flow. This approach combined the finite element method with classical thin shell theory, using displacement functions derived from the exact solutions of Sanders' shell equilibrium equations for conical shells. The ring-stiffened conical shell was divided into stiffened and unstiffened segments. The velocity potential and Bernoulli's equations used to calculate the fluid pressure acting on the wall structure, resulting in the calculation of three forces (inertial, centrifugal, Coriolis) in the case of flowing fluid. The mass, damping, and stiffness matrices were also calculated using exact analytical integration. To the best of the authors' knowledge, this paper presents the first comparison between stiffened and unstiffened shells subjected to flowing fluid. An investigation into the geometric parameters of ring-stiffened conical shells, including boundary conditions and the number of rings, yields the following insights: (1) Stiffeners induce higher frequencies compared to unstiffened shells, highlighting the significance of stiffener configuration on the free vibration characteristics of these structures; (2) A higher number of rings increases the dimensionless frequency for fluid-filled ($U_f = 0$) conical shells for all boundary conditions. However, the critical flow discharge is influenced by the circumferential mode number and displays unpredictable behavior depending on the specific boundary conditions; (3) The effect of the semi-vertex angle on the frequency response is evident, with an increase in the vertex angle leading to a decrease in critical flow discharge and a decrease in the dimensionless frequency for a fluid-filled shell. This approach can be effectively employed during the initial design phase, wherein various boundary conditions and configurations need to be tested in order to identify the optimal design.

CRediT authorship contribution statement

Mohammadamin Esmaeilzadehazimi: Writing – original draft, Visualization, Validation, Software, Methodology, Investigation, Formal analysis, Data curation, Conceptualization, Writing – review & editing. **Aouni A. Lakis:** Writing – review & editing, Validation, Supervision, Resources, Project administration, Methodology. **Mohammad Toorani:** Writing – review & editing, Visualization, Validation, Supervision, Formal analysis, Data curation.

Declaration of competing interest

The authors declare that they have no known competing financial interests or personal relationships that could have appeared to influence the work reported in this paper.

Data availability

Data will be made available on request.

References

[1] Ulric S. Lindholm, William C.L. Hu, Non-symmetric transverse vibrations of truncated conical shells, Int. J. Mech. Sci. 8 (9) (1966) 561–579.
[2] A.H. Sofiyev, M.H. Omurtag, E. Schnack, The vibration and stability of orthotropic conical shells with non-homogeneous material properties under a hydrostatic pressure, J. Sound Vib. 319 (3–5) (2009) 963–983.
[3] A.M.I. Sweedan, A.A. El Damatty, Experimental identification of the vibration modes of liquid-filled conical tanks and validation of a numerical model, Earthq. Eng. Struct. Dyn. 32 (9) (2003) 1407–1430.
[4] Mauro Caresta, Nicole J. Kessissoglou, Vibration of fluid loaded conical shells, J. Acoust. Soc. Am. 124 (4) (2008) 2068–2077.
[5] M. Rahmanian, R.D. Firouz-Abadi, E. Cigeroglu, Free vibrations of moderately thick truncated conical shells filled with quiescent fluid, J. Fluids Struct. 63 (2016) 280–301.
[6] M. Amabili, M.P. Paidoussis, A.A. Lakis, Vibrations of partially filled cylindrical tanks with ring-stiffeners and flexible bottom, J. Sound Vib. 213 (2) (1998) 259–299.
[7] Young-Wann Kim, Young-Shin Lee, Sung-Ho Ko, Coupled vibration of partially fluid-filled cylindrical shells with ring stiffeners, J. Sound Vib. 276 (3–5) (2004) 869–897.
[8] A.A. Jafari, M. Bagheri, Free vibration of non-uniformly ring stiffened cylindrical shells using analytical, experimental and numerical methods, Thin-Walled Struct. 44 (1) (2006) 82–90.
[9] C.T.F. Ross, W.D. Richards, The vibration of ring-stiffened cones under external water pressure, Proc. Inst. Mech. Eng. C 208 (3) (1994) 177–185.
[10] Meixia Chen, Cong Zhang, Xiangfan Tao, Naiqi Deng, Structural and acoustic responses of a submerged stiffened conical shell, Shock Vib. 2014 (2014).
[11] Victor Isadore Weingarten, Free vibrations of ring-stiffened conical shells, AIAA J. 3 (8) (1965) 1475–1481.
[12] Z. Mecitoğlu, Vibration characteristics of a stiffened conical shell, J. Sound Vib. 197 (2) (1996) 191–206.
[13] D.M. Raj, R. Narayanan, A.G. Khadakkar, V. Paramasivam, Effect of ring stiffeners on vibration of cylindrical and conical shell models, J. Sound Vib. 179 (3) (1995) 413–426.
[14] Otto E. Crenwelge Jr., D. Muster, Free vibrations of ring-and-stringer-stiffened conical shells, J. Acoust. Soc. Am. 46 (1B) (1969) 176–185.
[15] M. Talebitooti, M. Ghayour, S. Ziaei-Rad, R. Talebitooti, Free vibrations of rotating composite conical shells with stringer and ring stiffeners, Arch. Appl. Mech. 80 (2010) 201–215.
[16] Kun Xie, Meixia Chen, Naiqi Deng, Wenchao Jia, Free and forced vibration of submerged ring-stiffened conical shells with arbitrary boundary conditions, Thin-Walled Struct. 96 (2015) 240–255.
[17] Ming Liu, Jun Liu, Yuansheng Cheng, Free vibration of a fluid loaded ring-stiffened conical shell with variable thickness, J. Vib. Acoust. 136 (5) (2014).
[18] Mohammadamin Esmaeilzadehazimi, Mehrdad Bakhtiari, Mohammad Toorani, Aouni A. Lakis, Numerical modeling and analysis of fluid-filled truncated conical shells with ring stiffeners, J. Fluids Struct. 127 (2024) 104121.
[19] Marco Amabili, Rinaldo Garziera, Vibrations of circular cylindrical shells with nonuniform constraints, elastic bed and added mass. Part II: Shells containing or immersed in axial flow, J. Fluids Struct. 16 (1) (2002) 31–51.
[20] Yongqi Ma, Yunxiang You, Ke Chen, Aichun Feng, Analysis of vibration stability of fluid conveying pipe on the two-parameter foundation with elastic support boundary conditions, J. Ocean Eng. Sci. (2022).
[21] M.P. Paidoussis, A.D. Mateescu, Dynamics of cylindrical shells containing fluid flows with a developing boundary layer, AIAA J. 25 (6) (1987) 857–863.
[22] Chang Jeng-Shian, Chiou Wen-Jiann, Natural frequencies and critical velocities of fixed-fixed laminated circular cylindrical shells conveying fluids, Comput. Struct. 57 (5) (1995) 929–939.
[23] M.P. Païdoussis, J.-P. Denise, Flutter of thin cylindrical shells conveying fluid, J. Sound Vib. 20 (1) (1972) 9–26.
[24] Marco Amabili, Kostas Karagiozis, Michael P. Païdoussis, et al., Effect of geometric imperfections on shells conveying fluid, in: Proceedings of the 9th International Conference on Flow-Induced Vibrations–FIV2008, 2008, pp. 317–322.
[25] Mahdi Bayrami Atashgah, Mehdi Iranmanesh, Alireza Mojtahedi, et al., Developing a simplified method to investigate the dynamic behavior of fluid conveying pipes under mean internal pressure, Math. Probl. Eng. 2022 (2022).
[26] Huijie Shen, Jihong Wen, Dianlong Yu, Xisen Wen, Stability of clamped-clamped periodic functionally graded material shells conveying fluid, J. Vib. Control 21 (15) (2015) 3034–3046.
[27] R.D. Firouz-Abadi, M.A. Noorian, H. Haddadpour, A fluid–structure interaction model for stability analysis of shells conveying fluid, J. Fluids Struct. 26 (5) (2010) 747–763.
[28] Ravikiran Kadoli, N. Ganesan, Free vibration and buckling analysis of composite cylindrical shells conveying hot fluid, Compos. Struct. 60 (1) (2003) 19–32.
[29] A. Selmane, Aouni A. Lakis, Vibration analysis of anisotropic open cylindrical shells subjected to a flowing fluid, J. Fluids Struct. 11 (1) (1997) 111–134.
[30] Yuzhen Zhao, Dike Hu, Song Wu, Xinjun Long, Yongshou Liu, Dynamics of axially functionally graded conical pipes conveying fluid, J. Mech. 37 (2021) 318–326.
[31] S.A. Bochkarev, V.P. Matveenko, Natural vibrations and stability of shells of revolution interacting with an internal fluid flow, J. Sound Vib. 330 (13) (2011) 3084–3101.
[32] Michael P. Païdoussis, Ahmed R. Abdelbaki, M. Faisal Javed Butt, Mohammad Tavallaeinejad, Kyriakos Moditis, Arun K. Misra, Meyer Nahon, Joe L. Ratigan, Dynamics of a cantilevered pipe subjected to internal and reverse external axial flow: a review, J. Fluids Struct. 106 (2021) 103349.

[33] A.A. Lakis, P. Van Dyke, H. Ouriche, Dynamic analysis of anisotropic fluid-filled conical shells, J. Fluids Struct. 6 (2) (1992) 135–162.
[34] D. Senthil Kumar, N. Ganesan, Dynamic analysis of conical shells conveying fluid, J. Sound Vib. 310 (1–2) (2008) 38–57.
[35] Y. Kerboua, A.A. Lakis, M. Hmila, Vibration analysis of truncated conical shells subjected to flowing fluid, Appl. Math. Model. 34 (3) (2010) 791–809.
[36] H. Bagheri, Y. Kiani, M.R. Eslami, Free vibration of conical shells with intermediate ring support, Aerosp. Sci. Technol. 69 (2017) 321–332.
[37] M. Zarei, G.H. Rahimi, M. Hemmatnezhad, Free vibrational characteristics of grid-stiffened truncated composite conical shells, Aerosp. Sci. Technol. 99 (2020) 105717.
[38] Kun Xie, Meixia Chen, Linke Zhang, Wencheng Li, Wanjing Dong, A unified semi-analytic method for vibro-acoustic analysis of submerged shells of revolution, Ocean Eng. 189 (2019) 106345.
[39] Chunyu Zhang, Guoyong Jin, Zhihao Wang, Yao Sun, Dynamic stiffness formulation and vibration analysis of coupled conical-ribbed cylindrical-conical shell structure with general boundary condition, Ocean Eng. 234 (2021) 109294.
[40] Jiang-hai Wu, Yu-dong Sun, An exact solution for vibration analysis of pipe coupled with conical-ring stiffened cylindrical shells with arbitrary boundary condition, Ocean Eng. 266 (2022) 112861.
[41] Mohammad Javad Bayat, Amin Kalhori, Masoud Babaei, Kamran Asemi, Natural frequency characteristics of stiffened FG multilayer graphene-reinforced composite plate with circular cutout resting on elastic foundation, Int. J. Struct. Stab. Dyn. (2023) 2450202.
[42] Yuhua Zhou, Yanhu Zhang, Brighton Nyasha Chirukam, Jianwei Li, Congshan Lu, Masoud Babaei, Kamran Asemi, Free vibration analyses of stiffened functionally graded graphene-reinforced composite multilayer cylindrical panel, Mathematics 11 (17) (2023) 3662.
[43] Amin Kalhori, Mohammad Javad Bayat, Kamran Asemi, Buckling analysis of stiffened functionally graded multilayer graphene platelet reinforced composite plate with circular cutout embedded on elastic support subjected to in-plane normal and shear loads, Results Eng. 20 (2023) 101563.
[44] S. Zghal, A. Frikha, F. Dammak, Static analysis of functionally graded carbon nanotube-reinforced plate and shell structures, Compos. Struct. 176 (2017) 1107–1123.
[45] S. Zghal, A. Frikha, F. Dammak, Free vibration analysis of carbon nanotube-reinforced functionally graded composite shell structures, Appl. Math. Model. 53 (2018) 132–155.
[46] S. Zghal, A. Frikha, F. Dammak, Mechanical buckling analysis of functionally graded power-based and carbon nanotubes-reinforced composite plates and curved panels, Composites B 150 (2018) 165–183.
[47] S. Trabelsi, A. Frikha, S. Zghal, F. Dammak, Thermal post-buckling analysis of functionally graded material structures using a modified FSDT, Int. J. Mech. Sci. 144 (2018) 74–89.
[48] A. Frikha, S. Zghal, F. Dammak, Finite rotation three and four nodes shell elements for functionally graded carbon nanotubes-reinforced thin composite shells analysis, Comput. Methods Appl. Mech. Engrg. 329 (2018) 289–311.
[49] S. Trabelsi, A. Frikha, S. Zghal, F. Dammak, A modified FSDT-based four nodes finite shell element for thermal buckling analysis of functionally graded plates and cylindrical shells, Eng. Struct. 178 (2019) 444–459.
[50] S. Zghal, F. Dammak, Buckling responses of porous structural components with gradient power-based and sigmoid material variations under different types of compression loads, Compos. Struct. 273 (2021) 114313.
[51] Souhir Zghal, Sourour Trabelsi, Fakhreddine Dammak, Post-buckling behavior of functionally graded and carbon-nanotubes based structures with different mechanical loadings, Mech. Based Des. Struct. Mach. 50 (9) (2022) 2997–3039.
[52] Najah Joueid, Souhir Zghal, Mouldi Chrigui, Fakhreddine Dammak, Thermoelastic buckling analysis of plates and shells of temperature and porosity dependent functionally graded materials, Mech. Time-Dependent Mater. (2023) 1–43.
[53] J. Lyell Sanders, An Improved First-Approximation Theory for Thin Shells, Vol. 24, US Government Printing Office, 1960.
[54] Michael P. Nemeth, An In-Depth Tutorial on Constitutive Equations for Elastic Anisotropic Materials, Technical report, 2011.
[55] Autar K. Kaw, Mechanics of Composite Materials, CRC Press, 2005.
[56] Daryl L. Logan, A First Course in the Finite Element Method, Cengage Learning, 2016.
[57] M.D. Nurul Izyan, K.K. Viswanathan, Z.A. Aziz, Jang Hyun Lee, K. Prabakar, Free vibration of layered truncated conical shells filled with quiescent fluid using spline method, Compos. Struct. 163 (2017) 385–398.
[58] S. Graham Kelly, Advanced Vibration Analysis, CRC Press, 2006.
[59] Marco Amabili, Nonlinear Vibrations and Stability of Shells and Plates, Cambridge University Press, 2008.
[60] Xinping Zhou, Vibration and stability of ring-stiffened thin-walled cylindrical shells conveying fluid, Acta Mech. Solida Sin. 25 (2) (2012) 168–176.